IOP Publishing Plasma Sources Science and Technology
Plasma Sources Sci. Technol. **33** (2024) 055006 (21pp) https://doi.org/10.1088/1361-6595/ad4238

A novel state-resolved actinometry method to determine the nitrogen atom number density in the ground state and intra-shell excited states in low-pressure electron cyclotron resonance plasmas

Xi-Ming Zhu[1,*], Lu Wang[1,*], Yan-Fei Wang[1], Yang Wang[2], Da-Ren Yu[1] and Klaus Bartschat[3]

[1] School of Energy Science and Engineering, Harbin Institute of Technology, Harbin, Heilongjiang 150001, People's Republic of China
[2] School of Physics, Harbin Institute of Technology, Harbin, Heilongjiang 150001, People's Republic of China
[3] Department of Physics and Astronomy, Drake University, Des Moines, IA 50311, United States of America

E-mail: simon.ximing.zhu@outlook.com and hans.lu.wang@outlook.com

Received 8 January 2024, revised 16 April 2024
Accepted for publication 23 April 2024
Published 7 May 2024

Abstract

The active-particle number density is a key parameter for plasma material processing, space propulsion, and plasma-assisted combustion. The traditional actinometry method focuses on measuring the density of the atoms in the ground state, but there is a lack of an effective optical emission spectroscopy method to measure intra-shell excited-state densities. The latter atoms have chemical selectivity and higher energy, and they can easily change the material morphology as well as the ionization and combustion paths. In this work, we present a novel state-resolved actinometry (SRA) method, supported by a krypton line-ratio method for the electron temperature and density, to measure the number densities of nitrogen atoms in the ground and intra-shell excited states. The SRA method is based on a collisional-radiative model, considering the kinetics of atomic nitrogen and krypton including their excited states. The densities measured by our method are compared with those obtained from a dissociative model in a miniature electron cyclotron resonance (ECR) plasma source. Furthermore, the saturation effect, in which the electron density remains constant due to the microwave propagation in an ECR plasma once the power reaches a certain value, is used to verify the electron density measured by the line-ratio method. An ionization balance model is also presented to examine the measured electron temperature. All the values obtained with the different methods are in good agreement with each other, and hence a set of verified rate coefficient data used in our method can be provided. A novel concept, the 'excited-state system', is presented to quickly

* Authors to whom any correspondence should be addressed.

build an optical diagnostic method based on the analysis of quantum number propensity and selection rules.

Supplementary material for this article is available online

Keywords: state-resolved actinometry, nitrogen plasma, CR model, ECR ion source

1. Introduction

Measuring the number densities of active atoms and radicals has been of interest for a long time, due to their chemical selectivity and high energy. These atoms and radicals can induce changes in the reaction paths, such as promoting the rate of formatting film in plasma material processing, changing the ionization path in electron propulsion devices, and reducing the delay time of plasma ignition in plasma-assisted combustion systems [1–7].

Based on the light-source induced spectroscopic technologies, including single/two-photon absorption laser-induced fluorescence (LIF and TALIF) and absorption spectrum (AS) are powerful tools for *in situ* time- and space- resolved atomic atoms and radicals, such as for H, O, N, NO, OH and O_3 [8–12]. These technologies can obtain the densities of interest by simple equations. However, the frequencies of the single photon generated by LIF fall into the vacuum ultraviolet (VUV) region, thereby posing a significant problem to propagation in most practical environments. The improved TALIF technology tends to employ expensive ps/fs-lasers to eliminate unwanted photolytic production particles. Also, the AS is only reliable in the case of sufficient high optical depth [13, 14]. Compared with the above technologies, optical emission spectroscopy (OES) is the most promising for realistic industrial applications, especially in enclosed devices, i.e. the industrial chamber for material processing and the discharge chamber of the electron propulsion devices, due to its low-cost equipment and spontaneous radiation nature [15–19]. In order to obtain the absolute density, the OES method must be supported with kinetic investigations, i.e. the actinometry method, to determine the particle density of interest from the measured emission lines. It is worth noting that the relative calibrated OES experiments are preferred to be used compared to those with absolute calibration since the latter must consider the solid angle of the optical system [20, 21].

There are two main steps to apply this approach: one is adding a trace actinometer (e.g. a noble gas, often Ar) to the plasma, and the other is choosing emission lines from the actinometer and the measured atomic emitting state to build the function relating the particle number density with the above measured emission lines. Note that the excitation thresholds of the chosen lines must be close enough to avoid the actinometric coefficient (the ratio relationship of the rate coefficients) being affected by the electron temperature. The density can then be determined because it is proportional to the ratio of the above lines, due to the population of the excited states being assumed to have been excited from the ground state.

Some studies used this traditional actinometry method to obtain the densities of N, O, and F atoms [22–26]. However, the assumption that excitation from the ground state dominates the population of the measured states is incorrect in some operating conditions. For example, the population of the upper states resulting in O(777 nm) emission is dominated by dissociative excitation, which leads to a disagreement with measurements performed in two-photo absorption LIF experiments [27, 28]. To solve this problem, the reaction kinetics needs to be considered in the actinometry method, i.e. dissociative excitation and excitation from the ground state are both included to describe the population of the excited states from the chosen emission lines [29–31]. Furthermore, the plasma properties need to be investigated in detail, since the actinometric coefficient cannot remain constant over a wide range of discharge conditions [32, 33]. Even though the above actinometry method has successfully determined some particle densities, it can only measure those in the ground state. For particles with higher energy and chemical selectivity, referred to as 'intra-shell excited-state particles' below, there is a lack of an effective OES method to measure their densities.

In this work, we present a novel state-resolved actinometry (SRA) method to measure the number densities of nitrogen atoms in the ground state and intra-shell excited states, based on a collisional-radiative (CR) model coupling the kinetics between the observed particles and their excited states. The densities measured by our method are compared with those obtained from the dissociation model. Furthermore, we propose a line-ratio method using krypton lines to determine the electron density and temperature, and their values are verified by the saturation effect and the ionization balance model. In particular, we propose a novel concept, the 'excited-state system', to help in quickly building a diagnostic method for the parameters of interest.

This paper is structured as follows. In section 2, we describe the method used in this work. Section 3 introduces the experiment, while section 4 investigates the mapping relation of the line ratios and the dominant kinetic processes. Section 5 discusses the excited-state system concept and quantum number propensity/selection rules, the uncertainty of the SRA, and its applicability range. Conclusions are drawn in section 6. The rate coefficients and Einstein coefficients used in this paper will be made available through the LXCat database [34].

2. Methods

This section introduces our general CR model of nitrogen and krypton plasma (section 2.1), the SRA method (section 2.2),

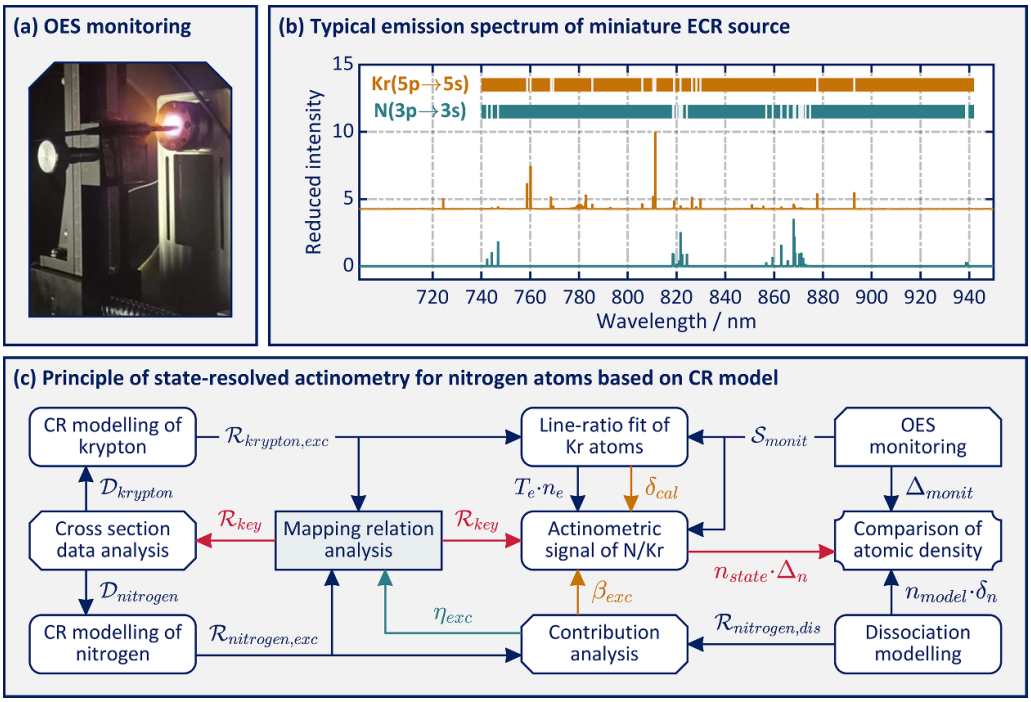

Figure 1. Principle of state-resolved actinometry for nitrogen atoms, based on the collisional-radiative model.

the OES line-ratios method for krypton (section 2.3), and the verification method for the above parameters (section 2.4).

Our method, depicted in figure 1, is a novel actinometry approach based on OES for measuring the nitrogen atom number density in the ground and intra-shell excited states. The method involves four main phases. First, a CR model for analyzing the reaction kinetics needs to be built, including the CR model of the nitrogen and krypton plasma studied in the present work. Second, a mapping relation is carried out to find the line ratios that are sensitive to the measured parameters. A contribution analysis is also needed to find the coupling relationship between the measured particles and the emission lines. Third, after the OES monitoring experiment, we can obtain the parameters of interest by fitting the experimental and modeled line ratios. The experiment also provides the emission signals for the density measurement. At last, a dissociation model is used to verify the results.

In the first phase, creating a database of nitrogen and krypton plasma, denoted as '$\mathcal{D}_{\text{krypton}}$' and '$\mathcal{D}_{\text{nitrogen}}$', respectively, is a crucial step. The two databases separately provide cross sections to the molecular nitrogen and atomic krypton CR models. In the second phase, a mapping relation analysis is carried out to find the key reactions $\mathcal{R}_{\text{key}}$, which are sensitive to the measured parameters from the reaction set of nitrogen and krypton ($\mathcal{R}_{\text{nitrogen,exc}}$, $\mathcal{R}_{\text{krypto,exc}}$), by a percentage of contribution (η_{exc}) analysis. In the third phase, the OES experiment, depicted in figures 1(a) and (b), exhibits the location of the monitor and the typical spectrum. The electron density (n_{e}), and temperature (T_{e}) are determined by fitting the line ratio for the Kr atom from the OES monitoring ($\mathcal{S}_{\text{monit}}$) and the model. Supported by the measured n_{e} and T_{e}, the number density of nitrogen can be determined by building the function related to the actinometric signal and the rate coefficients of the key reactions. Furthermore, it is worth noting that the uncertainty of the measured values, Δ_n, consists of those from the experiment (Δ_{monit}), the fitted electron temperature and density (δ_{cal}), and the approximate deviation of the actinometry equations caused by the variation of the dominant excitation kinetics (β_{exc}). At last, the dissociation model is built, based on the kinetics of the dissociation processes ($\mathcal{R}_{\text{nitrogen,dis}}$). Finally, the calculated values are compared with those obtained from the SRA method, with the uncertainty denoted by δ_n.

2.1. General CR model

The rate balance equations describe the behavior of particles in the plasma based on the reaction kinetics considered in the CR model. Their general expressions will be given in this section.

Under typical low-pressure electron cyclotron resonance (ECR) discharge conditions (pressure 0.1–1 Pa, electron density 10^{10}–3×10^{11} cm^{-3}, electron temperature 5–25 eV), the important processes involved are electron-impact, (including dissociation, dissociative excitation, excitation from the ground and metastable states, ionization), radiation, absorption, and diffusion processes. Based on the above processes, table 1 presents the equations that describe the creation and destruction of the species of interest.

Equation (1) is the rate balance equation, with 'col', 'rad', 'abs', and 'wall' referring to collision, radiation, absorption, and diffusion-controlled quenching at the wall processes. The reaction rate of the collision term $R_{y\to x}^{col,e}$ is written in equation (2), determined by the electron density n_{e}, the particle density n_y, and the rate coefficient Q. The expression for Q is given in equation (3). It is determined by the

Table 1. Rate balance equations are used for the CR model.

	Equation	Describe
Equation (1)	$\sum_{y\neq x} R^{\mathrm{col}}_{y\to x} + \sum_{y>x} R^{\mathrm{rad}}_{y\to x} + \sum_{y<x} R^{\mathrm{abs}}_{y\to x} = \sum_{y\neq x} R^{\mathrm{col}}_{x\to y} + \sum_{y<x} R^{\mathrm{rad}}_{x\to y} + \sum_{y>x} R^{\mathrm{abs}}_{x\to y} + R^{\mathrm{wall}}_{x}$	R: reaction rate x, y: state considered in the CR model
Equation (2)	$R^{\mathrm{col,e}}_{y\to x} = n_{\mathrm{e}} \cdot n_y \cdot Q^{\mathrm{e}}_{y\to x}$	n_{e}: electron density n_y: particle density Q: electron-impact rate coefficient
Equation (3)	$Q^{\mathrm{e}}_{y\to x} = \int_{E_0}^{\infty} \sigma^{\mathrm{e}}_{y\to x}(E_{\mathrm{e}}) \cdot \sqrt{\frac{2E_{\mathrm{e}}}{m_{\mathrm{e}}}} \cdot g_{\mathrm{e}}(E_{\mathrm{e}}) \cdot \mathrm{d}E_{\mathrm{e}}$	$\sigma^{\mathrm{e}}_{y\to x}$: cross-section from y to x E_{e}: electron kinetic energy m_{e}: electron mass g_{e}: EEDF
Equation (4)	$g_{\mathrm{e}}(E_{\mathrm{e}}) = \frac{2}{\sqrt{\pi}} T_{\mathrm{e}}^{-3/2} \sqrt{E} \mathrm{e}^{-E/T_{\mathrm{e}}}$	E: electron energy T_{e}: effective electron temperature
Equation (5)	$R^{\mathrm{rad}}_{y\to x} - R^{\mathrm{abs}}_{x\to y} = \Gamma_{x\to y}(n_x) \cdot A_{y\to x} \cdot n_y$	y, n_y: upper state and density x, n_x: lower state and density $A_{y\to x}$: Einstein coefficient
Equation (6)	$\Gamma(\tau) = \frac{2-\exp(-p\cdot\tau)}{1+(q\cdot\tau)^k}$	Γ: escape factor τ: optical depth of plasma
Equation (7)	$R^{\mathrm{wall}}_{x,n} = K_{x,n} \cdot n_x$, $R^{\mathrm{wall}}_{x,+} = K_{x,+} \cdot n_x$	$R^{\mathrm{wall}}_{x,n}$: neutral loss rate due to diffusion $R^{\mathrm{wall}}_{x,+}$: ion loss rate due to diffusion
Equation (8)	$K_{x,n} = \left[\left(\frac{\Lambda_n^2}{D_n}\right)^{-1} + \left(\frac{2V(2-\gamma_n)}{A v_n \gamma_n}\right)\right]^{-1}$ $\Lambda_n = \left[\left(\frac{\pi}{L}\right)^2 + \left(\frac{2.405}{R}\right)^2\right]^{-1/2}$	$K_{x,n}$: loss frequency of neutral D_n: diffusion coefficient γ_n: sticking coefficient v_n: mean neutral speed Λ_n: effective diffusion length V, A: volume and wall surface area L, R: radius and length
Equation (9)	$K_{x,+} = 2u_{\mathrm{B}} \frac{R^2 h_L + RLh_R}{R^2 L}$	$K_{x,+}$: loss frequency for the ions u_{B}: Bohm velocity h_L: edge-to-center density ratio in axial h_R: edge-to-center density ratio in radial

electron-impact cross section $\sigma^{e}_{y\to x}$ and the electron energy distribution function (EEDF) g_{e}. A Maxwellian distribution is assumed in the model, as shown in equation (4) [35]. The radiation and absorption terms in the rate balance equation are written in equation (5), where the escape factor Γ used is shown in equation (6). The coefficients of the escape factor are found in [36]. The diffusion term includes both neutral and ion diffusion, $R^{wall}_{x,n}$ and $R^{wall}_{x,+}$. The loss frequency of the neutral $K_{x,n}$ can be found in equation (8), and those of the ion $K_{x,+}$ are given in equation (9). The densities of the particles of interest can be obtained by solving the rate balance equation.

A complete reaction set and the corresponding cross sections included in the CR model of the nitrogen plasma are given in appendix A, and those of the krypton plasma in appendix B. Once the reaction set and the cross sections are provided, one can build the CR model using equations (1)–(9) in table 1. It is worth noting that the rate equation of the dissociation model and the ionization model can also be described by the equations given in table 1. They will be introduced in detail in section 2.4.

2.2. SRA method to determine the nitrogen atom density

Our SRA method is based on the investigation of the kinetics in a nitrogen plasma described by the CR model. The CR model focuses on the kinetics of the $2p^3\,{}^4S^\circ$, $2p^3\,{}^2D^\circ$, and $2p^3\,{}^2P^\circ$ states, as well as selected 3p states of atomic nitrogen, also listed in table 2. Among these states, we pay attention to the $2p^2(^3P)3p\ {}^4S^\circ$, $2p^2(^3P)3p\ {}^2D^\circ$, and $2p^2(^3P)3p\ {}^2P^\circ$ states, due to their number densities being related to those of the $N(2p^3\,{}^4S^\circ)$, $N(2p^3\,{}^2D^\circ)$, $N(2p^3\,{}^2P^\circ)$ states, respectively. Tables 3 and 4 list the reaction set of the three key 3p states. We obtain the densities of the states considered in the model

Table 2. N levels in the present CR model.

	State	Term	E (eV)	Symbol
1	$2s^22p^3$	$^4S^\circ$	0	N($^4S^\circ$)
2	$2s^22p^3$	$^2D^\circ$	2.384	N($^2D^\circ$)
3	$2s^22p^3$	$^2P^\circ$	3.576	N($^2P^\circ$)
4	$2s^22p^2(^3P)3s$	^4P	10.332	N(3s ^4P)
5	$2s^22p^2(^3P)3s$	^2P	10.687	N(3s ^2P)
6	$2s2p^4$	^4P	10.927	N($2p^4$ ^4P)
7	$2s^22p^2(^3P)3p$	$^2S^\circ$	11.603	N(3p $^2S^\circ$)
8	$2s^22p^2(^3P)3p$	$^4D^\circ$	11.758	N(3p $^4D^\circ$)
9	$2s^22p^2(^3P)3p$	$^4P^\circ$	11.842	N(3p $^4P^\circ$)
10	$2s^22p^2(^3P)3p$	$^4S^\circ$	11.996	N(3p $^4S^\circ$)
11	$2s^22p^2(^3P)3p$	$^2D^\circ$	12.006	N(3p $^2D^\circ$)
12	$2s^22p^2(^3P)3p$	$^2P^\circ$	12.125	N(3p $^2P^\circ$)

Table 3. Set of nitrogen reactions involving the ground state, the intra-shell excited states, and the key 3p states.

	Reactions	Rate coefficients (cm^3 s^{-1})	References
R_1	$e + N_2(X) \rightarrow e + N(^4S^\circ) + N(^4S^\circ)$	$1.79 \times 10^{-9} \times T_e^{0.639} \times \exp(-9.76/T_e)$	[37, 38]
R_2	$e + N_2(X) \rightarrow e + N(^4S^\circ) + N(^2D^\circ)$	$5.32 \times 10^{-9} \times T_e^{0.483} \times \exp(-12.14/T_e)$	[37, 38]
R_3	$e + N_2(X) \rightarrow e + N(^4S^\circ) + N(^2P^\circ)$	$2.85 \times 10^{-9} \times T_e^{0.406} \times \exp(-12.33/T_e)$	[37, 38]
R_4	$e + N_2(X) \rightarrow e + N(^4S^\circ) + N(3p^4S^\circ)$	$9.54 \times 10^{-12} \times T_e^{0.532} \times \exp(-21.75/T_e)$	[39]
R_5	$e + N_2(X) \rightarrow e + N(^4S^\circ) + N(3p^2D^\circ)$	$6.02 \times 10^{-11} \times T_e^{0.494} \times \exp(-21.76/T_e)$	[39]
R_6	$e + N_2(X) \rightarrow e + N(^4S^\circ) + N(3p^2P^\circ)$	$3.12 \times 10^{-11} \times T_e^{0.489} \times \exp(-21.88/T_e)$	[39]
R_7	$e + N(^4S) \leftrightarrow e + N(^2D^\circ)$	$2.29 \times 10^{-8} \times T_e^{-0.390} \times \exp(-2.38/T_e)$	[40]
R_8	$e + N(^4S) \leftrightarrow e + N(^2P^\circ)$	$7.95 \times 10^{-9} \times T_e^{-0.445} \times \exp(-3.58/T_e)$	[40]
R_9	$e + N(^4S) \leftrightarrow e + N(3p^4S^\circ)$	$4.54 \times 10^{-10} \times T_e^{0.130} \times \exp(-11.99/T_e)$	[40]
R_{10}	$e + N(^4S) \leftrightarrow e + N(3p^2D^\circ)$	$8.60 \times 10^{-10} \times T_e^{-0.543} \times \exp(-12.00/T_e)$	[40]
R_{11}	$e + N(^4S) \leftrightarrow e + N(3p^2P^\circ)$	$4.71 \times 10^{-10} \times T_e^{-0.717} \times \exp(-12.12/T_e)$	[40]
R_{12}	$e + N(^2D) \leftrightarrow e + N(3p^4S^\circ)$	$1.91 \times 10^{-10} \times T_e^{-0.495} \times \exp(-9.61/T_e)$	[40]
R_{13}	$e + N(^2D) \leftrightarrow e + N(3p^2D^\circ)$	$3.00 \times 10^{-9} \times T_e^{-0.185} \times \exp(-9.62/T_e)$	[40]
R_{14}	$e + N(^2D) \leftrightarrow e + N(3p^2P^\circ)$	$4.34 \times 10^{-10} \times T_e^{-0.175} \times \exp(-9.74/T_e)$	[40]
R_{15}	$e + N(^2P) \leftrightarrow e + N(3p^4S^\circ)$	$1.80 \times 10^{-10} \times T_e^{-0.698} \times \exp(-8.42/T_e)$	[40]
R_{16}	$e + N(^2P) \leftrightarrow e + N(3p^2D^\circ)$	$1.03 \times 10^{-9} \times T_e^{-0.158} \times \exp(-8.42/T_e)$	[40]
R_{17}	$e + N(^2P) \leftrightarrow e + N(3p^2P^\circ)$	$3.66 \times 10^{-9} \times T_e^{-0.194} \times \exp(-8.55/T_e)$	[40]

Table 4. Other sets of nitrogen reactions involving optical transitions and diffusion-controlled quenching at the wall.

	Reactions	Einstein coefficient (s^{-1})	References
R_{18}	$N(3p^4S^\circ) \rightarrow N(3s^4P) + h\nu$	3.71×10^7	[41]
R_{19}	$N(3p^2D^\circ) \rightarrow N(3s^2P) + h\nu$	2.50×10^7	[41]
R_{20}	$N(3p^2P^\circ) \rightarrow N(3s^2P) + h\nu$	3.16×10^7	[41]
	Particles	Diffusion coefficient (cm^2 s^{-1})	References
R_{21}	$N(^4S^\circ) \rightarrow 1/2N_2(X)$	$2 \times 10^{19}/n_g$	[42–44]
R_{22}	$N(^2D^\circ) \rightarrow N(^4S^\circ)$	$6 \times 10^{18}/n_g$	[43, 45]
R_{23}	$N(^2P^\circ) \rightarrow N(^4S^\circ)$	$5 \times 10^{18}/n_g$	[43, 45]
R_{24}	$N(3p) \rightarrow N(^4S^\circ)$	$5 \times 10^{18}/n_g$	[43, 45]

by solving the rate balance equations written in table 1, from which the contribution from the ground state and intra-shell excited states to the population of the 3p states can be determined. Based on these, we can obtain the equations that describe the relationship between the measured states and the emission lines; they are listed in table 5. Equation (10) gives the general expression for measuring the densities of states in this work. It depends on the actinometric coefficient C_{act}^{y}, the excitation coefficient α_y, and the so-called actinometric signal (I_x/I_{act}). In this work, n_y ($y = 2p^3\,^4S^\circ$, $2p^3\,^2D^\circ$, $2p^3\,^2P^\circ$) denotes the measured densities of the ground state and two intra-shell excited states from the special actinometric signals. In equations (10)–(13), for measuring the $2p^3\,^4S^\circ$ state, $y = 2p^3\,^4S^\circ$ and $x = 2p^2(^3P)3p\ ^4S^\circ$, but for N($2p^3\,^2D^\circ$) and N($2p^3\,^2P^\circ$) states, $y = 2p^3\,^2D^\circ$, $x = 2p^2(^3P)3p\ ^2D^\circ$ and $y = 2p^3\,^2P^\circ$, $x = 2p^2(^3P)3p\ ^2P^\circ$, respectively. Furthermore,

Table 5. Equations used to determine the number densities of N($2p^3\,{}^4S^\circ$), N($2p^3\,{}^2D^\circ$), N($2p^3\,{}^2P^\circ$).

	Equation	Description
Equation (10)	$\frac{n_y}{n_{\rm act}} = C^y_{\rm act}\frac{I_{\rm N(x)}}{I_{\rm Kr(x)}} - \frac{\alpha_y}{\xi}$	n_y: density of measured states $n_{\rm act}$: density of actinometry gas (act = Kr in this work) $I_{\rm N(x)}$: intensity of emission line from state x of N $I_{\rm Kr(x)}$: intensity of emission line from state x of Kr $C^{\rm y}_{act}$: ratio of rate coefficients for atomic excitation α_y: ratio of rate coefficients for molecular excitation and atomic excitation ξ: fraction of actinometer in the gas
Equation (11)	$C^y_{\rm act} = \frac{Q_{\rm Kr(gs)\to Kr(x)}}{Q_{\rm N(y)\to N(x)}}$	Q: rate coefficient Kr(gs): ground state of Kr Kr(x): excited state x of Kr N(x): excited state x of N N(y): excited state y of N
Equation (12)	$\alpha_y = \frac{Q_{\rm N_2(gs)\to N(x)}}{Q_{\rm N(y)\to N(x)}}$	N_2(gs): ground state of N_2
Equation (13)	$\xi = \frac{n_{\rm act}}{n_{\rm N_2}}$	$n_{\rm N2}$: density of molecular N_2

Kr(x) denotes the $4p^5(^2P^\circ_{3/2})5p^2[1/2]_0$ state in the above three cases.

As shown in table 5, the rate coefficient Q controls the actinometric coefficient $C^{\rm y}_{\rm act}$ and the excitation coefficient α_y. The expressions for the rate coefficients can be found in equation (2) of table 1. They are calculated according to the cross sections and the assumed EEDF (a Maxwell distribution is taken in this work; see [35]). There are six kinds of reaction kinetics considered in the CR model for the investigation of the key reactions affecting the population of the excited states in tables 3 and 4: (1) electron-impact dissociation processes (R_1–R_3); the total dissociation cross section was measured by Cosby [37], and the branching ratios for R_1–R_3 are assumed to be 0.5, 0.3, and 0.2, based on the predictions by Zipf *et al* [38]; (2) electron-impact dissociative excitation processes (R_4–R_6); the cross sections were measured by Filippelli *et al* [39]; (3) electron-impact excitation processes from the ground and metastable states (R_7–R_{17}); the cross sections were calculated by Wang *et al*, using the *B*-spline *R*-matrix-with preudostates method [40]; (4) spontaneous radiation (R_{18}–R_{20}); their Einstein coefficients are taken from NIST [41]; (5) diffusion processes (R_{21}–R_{23}); the diffusion coefficient D_n and the sticking coefficient γ can be found in [42–45].

2.3. Line-ratio method

The line-ratio method for measuring the electron density ($n_{\rm e}$) and temperature ($T_{\rm e}$) is based on the investigation of the excited states of Kr(5p). The states considered in our Kr CR model are listed in table B1. Note that $4p^5(^2P^\circ_{3/2})5p\ ^2[5/2]_3$, $4p^5(^2P^\circ_{3/2})5p\ ^2[1/2]_0$, $4p^5(^2P^\circ_{1/2})5p\ ^2[1/2]_0$, and $4p^5(^2P^\circ_{1/2})5p\ ^2[3/2]_2$ are the most important states in the CR model, since their populations distribution can be used to determine $n_{\rm e}$ and $T_{\rm e}$. This follows from the analysis of the line-ratio mapping relation. The reaction set involving the four Kr(5p) states is listed in table B2. The cross sections used in the Kr CR model are from measurements in Lin's group [46] and calculations in Bartschat's group [47], while the diffusion coefficients and the Einstein coefficients are from Kolts *et al* [48] and the NIST database [41]. We obtain the densities of the Kr(5p) states by solving the rate balance equations (equations (1)–(9) in table 1). After that, the emission intensity I can be calculated, since I is proportional to the excited-state densities. Two group line-ratios are defined to measure $n_{\rm e}$ and $T_{\rm e}$, as shown in table 6, i.e. $\gamma_{1,xy}$ for $n_{\rm e}$ (equation (14)) and $\gamma_{2,xy}$ for $T_{\rm e}$ (equation (15)). For simplification, the Kr states are written in Paschen notation instead of the J–K coupling scheme in table 6; the corresponding relationship between them is shown in table B1.

2.4. Verification method

2.4.1 Dissociation model. The dissociation model, based on the kinetics investigation of the $2p^3\,{}^4S^\circ$, $2p^3\,{}^2D^\circ$, and $2p^3\,{}^2P^\circ$ states of atomic nitrogen, includes the dissociation processes (R_1–R_3), the excitation processes (R_7–R_8), and the diffusion process (R_{21}–R_{24}). The cross sections for R_1–R_3 and R_7–R_8 were introduced in section 2.2. The diffusional losses of neutrals are estimated by an effective loss-rate coefficient $K_{\rm loss}$ (equation (8) in table 1); the coefficient D_n involved and the sticking coefficient can be found in [42–45]. The densities of the above three states can be determined by solving the rate-balance equations, a simplified expression of equation (1), i.e.

$$\sum_{y\neq x} R^{\rm col}_{y\to x} = R^{\rm wall}_{x,n}. \tag{16}$$

Here, 'col' denotes the electron-impact dissociation with y (N_2), and 'wall' is the neutral diffusion of x particles, specifically in the $2p^3\,{}^4S^\circ$, $2p^3\,{}^2D^\circ$, and $2p^3\,{}^2P^\circ$ states of atomic nitrogen. The reaction rate $R^{\rm col}_{x\to y}$ can be found in equations (2)–(4), and $R^{\rm wall}_{x,n}$ in equations (7)–(8).

Table 6. Line-ratios used to determine the electron density and temperature.

	Equation	Describe
Equation (14)	$\gamma_{1,xy} = \frac{I_{\mathrm{Kr(5p}x\mathrm{)}}}{I_{\mathrm{Kr(5p}y\mathrm{)}}} = \frac{Q_{\mathrm{Kr(gs)}\rightarrow\mathrm{Kr(5p}x\mathrm{)}}}{Q_{\mathrm{Kr(gs)}\rightarrow\mathrm{Kr(5p}y\mathrm{)}}} + \frac{n_{\mathrm{Kr(4s}x\mathrm{)}}}{n_{\mathrm{Kr(gs)}}} \frac{Q_{\mathrm{Kr(4s}x\mathrm{)}\rightarrow\mathrm{Kr(5p}x\mathrm{)}}}{Q_{\mathrm{Kr(gs)}\rightarrow\mathrm{Kr(5p}y\mathrm{)}}}$	$\gamma_{1,xy}$: line-ratio for n_e x, y: one of the 1s and 2p states gs: ground state Kr(5px): x refers to the $2p_9$ state Kr(4sx): x refers to the $1s_5$ state Kr(5py): y refers to the $2p_5$ state $I_{\mathrm{Kr(5p}x\mathrm{)}}$: intensity of the $2p_9 \rightarrow 1s_5$ transition (811.3 nm) $I_{\mathrm{Kr(5p}y\mathrm{)}}$: intensity of the $2p_5 \rightarrow 1s_4$ transition (758.7 nm) Q: rate coefficient n: density
Equation (15)	$\gamma_{2,xy} = \frac{I_{\mathrm{Kr(5p}x\mathrm{)}}}{I_{\mathrm{Kr(5p}y\mathrm{)}}} = \frac{Q_{\mathrm{Kr(gs)}\rightarrow\mathrm{Kr(5p}x\mathrm{)}}}{Q_{\mathrm{Kr(gs)}\rightarrow\mathrm{Kr(5p}y\mathrm{)}}}$	$\gamma_{2,xy}$: line-ratio for T_e Kr(5px): x refers to the $2p_2$ state Kr(5py): y refers to the $2p_1$ state $I_{\mathrm{Kr(5p}x\mathrm{)}}$: intensity of the $2p_2 \rightarrow 1s_2$ transition (826.3 nm) $I_{\mathrm{Kr(5p}y\mathrm{)}}$: intensity of the $2p_1 \rightarrow 1s_2$ transition (768.5 nm)

2.4.3. Saturation effect in the ECR plasma. The phenomenon of electron density (n_e) saturation ($\sim 2.2 \times 10^{11}$ cm^{-3}, 4.2 GHz frequency) is observed, i.e. n_e no longer increases with the absorbed power and inlet flow rate at the resonance position of our 2 cm miniature ECR ion source [49]. The value for n_e is derived from the relation

$$f_{pe} = \frac{1}{2\pi}\left(\frac{e^2 n_e}{\varepsilon_0 m}\right)^{1/2}. \tag{17}$$

Here, e is the electron charge, n_e is the electron density, ε_0 is the vacuum permittivity, m is the electron mass, and f_{pe} is the microwave frequency ~4.2 GHz.

2.4.3 Ionization balance model. This model is based on the continuity equation for the species, which describes the kinetics of N_2 ions in the average volume. It can be written as

$$\sum_{y\neq x} R^{\mathrm{col}}_{y\rightarrow x} = R^{\mathrm{wall}}_{x,+}. \tag{18}$$

Here, 'col' is the electron-impact dissociation with y (N_2), 'wall' is the ion diffusion of x (N_2^+). The reaction rate $R^{\mathrm{col}}_{x\rightarrow y}$ can be found in equations (2)–(4), and $R^+_{x,n}$ in equations (7) and (9). The ionization cross section are taken from recommended values of Itikawa *et al* [50], based on the measurements by Straub *et al* [51]. The latter are employed in many nitrogen plasma models [52–56].

3. Experiment

3.1. ECR plasma source

A schematic diagram of the experimental discharge devices is shown in figure 2. Experiments in the present work are performed on a miniature ECR plasma source with a diameter of 2 cm and an axial length of 4 mm. The schematic of the ECR source is also shown in figure 2. Details of the configuration of the ECR source were described by Koizumi *et al* [57], Yang *et al* [58], and Meng *et al* [49]. The discharge works using molecular nitrogen, whose flow rate (q) is either 0.2, 0.3, or 0.5 sccm. For the above three flow rates, the krypton actinometer is provided at 0.05 sccm, and the input microwave power (P_{in}) varies from 2 to 9 W. In our operating conditions, the dissociation degree can reach ~1%–2%.

3.2. Optical measurement

The emission from the plasma is recorded using an optical-fiber CCD spectrometer (FHR-1000, HORIBA Inc., wavelength range 200–1200 nm, resolution 0.05 nm, slit width 20 μm). As shown in figure 2, the optical probe coincides with the center line of the discharge chamber. A tungsten lamp was utilized as a dot source to investigate the spatial resolution of the optical probe. The angular resolution of the optical probe can reach ~1°, and the spatial resolution is better than 2 mm. The details of the method for determining the spatial resolution can refer to our previous paper [59]. The deuterium calibration lamp (~200–420 nm) and the halogen calibration lamp (~420–1100 nm) are used to calibrate the relative response of the optical systems. The emission lines of N(3p) and Kr(5p) are observed in the experiments used for the diagnostics.

4. Results

There are four main topics covered in this section. Firstly, the CR processes of the $4p^5(^2P^\circ_{3/2})5p\ ^2[5/2]_3$, $4p^5(^2P^\circ_{3/2})5p\ ^2[1/2]_0$, $4p^5(^2P^\circ_{1/2})5p\ ^2[3/2]_2$, and $4p^5(^2P^\circ_{1/2})5p\ ^2[1/2]_0$ states of atomic krypton are analyzed. The mapping relations for determining n_e (811.3 nm/758.7 nm) and T_e (826.3 nm/768.5 nm) are given. Secondly, based on the mapping relation, the measured values of n_e and T_e using the line-ratio method versus power and flow are given; among them, n_e is verified via the saturation effect of the ECR plasma source, while T_e is compared with the value obtained from the ionization model. After that, the key kinetic mechanisms

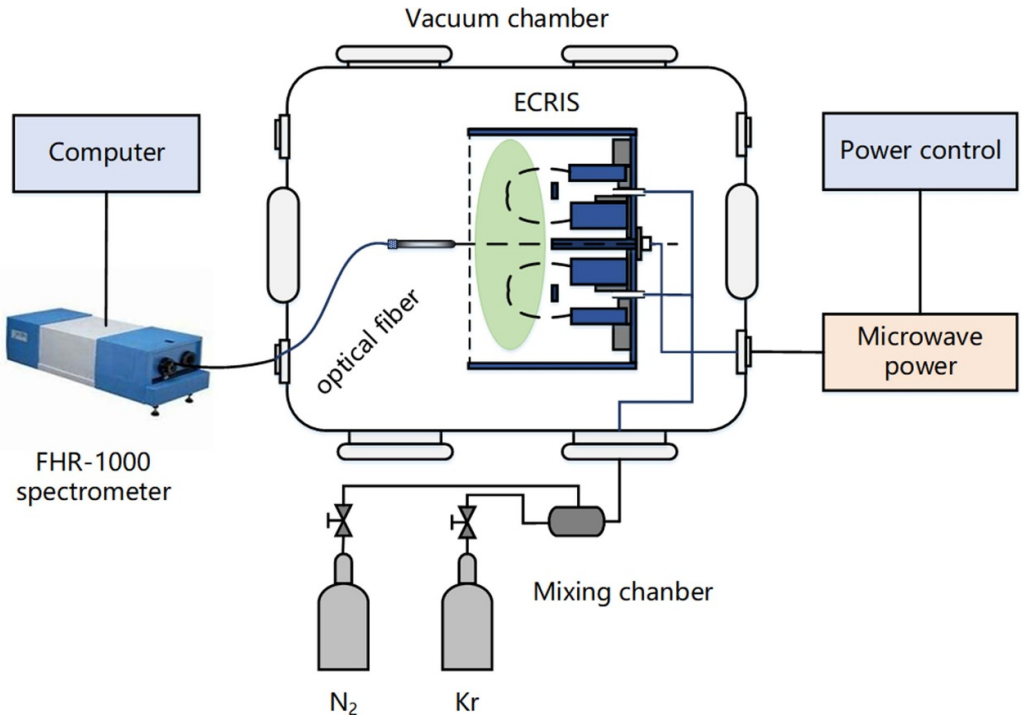

Figure 2. Schematic diagram of the experimental setup.

for measuring the number densities in the ground state and the intra-shell excited states are investigated. Lastly, the measured densities of the $2p^3\,{}^4S^\circ$, $2p^3\,{}^2D^\circ$, $2p^3\,{}^2P^\circ$ states of atomic nitrogen are compared with those calculated by the dissociation model.

4.1. Mapping relation for the electron density and temperature

From figures 3(a) and (c), it can be seen that the $4p^5(^2P^\circ_{3/2})5p\ ^2[1/2]_0$, $4p^5(^2P^\circ_{1/2})5p\ ^2[3/2]_2$, and $4p^5(^2P^\circ_{1/2})5p\ ^2[1/2]_0$ states of the Kr atom are mainly excited from the ground state, while the $4p^5(^2P^\circ_{3/2})5p\ ^2[5/2]_3$ state is not only generated by excitation from the ground state but also by excitation from metastable states. Because of this difference, the line-ratio γ_1 (811.3 nm/758.7 nm), has a strong n_e dependence as shown in figure 3(b), while the γ_2 ratio (826.3 nm/768.5 nm) has a strong T_e dependence seen in figure 3(d). Recall that the expressions for γ_1 and γ_2 are presented in table 6. Another reason for choosing γ_2 to obtain T_e is the fact that the energy dependences of the cross sections for the emitting states are very different. In particular, the cross section for $4p^5(^2P^\circ_{1/2})5p\ ^2[1/2]_0$ decreases more slowly than that for $4p^5(^2P^\circ_{1/2})5p\ ^2[3/2]_2$ above threshold, according to measurements in Lin's group [46]. By using the latter cross section, one can thus diagnose a larger range of T_e (∼5–20 eV), even though the threshold energy of the two states is close (∼0.1 eV). Furthermore, cascade effects have little influence on either of the two cross sections, as becomes evident by comparing the apparent and the direct cross sections. Consequently, our method can also be applied at higher discharge pressure (∼20 Pa). The highest pressure is determined by considering the reabsorption effect of the resonance radiation from the $4p^5(^2P^\circ_{3/2})5\ s\ ^2[1/2]^\circ_1$ state. Above this pressure, the resonance state significantly contributes to the $4p^5(^2P^\circ_{1/2})5p\ ^2[3/2]_2$ state, and the contribution is considerable with the ground-state excitation, resulting in the coronal model involved with the two emitting states for determining the electron temperature is not suitable.

4.2. Electron density and temperature versus the power and flow rate

Figure 4 depicts the electron density and temperature versus the input power and the nitrogen flow rate, respectively, obtained at the central region of the ECR plasma source. Figure 4(a) shows a density increase from 7×10^{10} cm^{-3} to 1.36×10^{11} cm^{-3}, as the power rises from 2 W to 5.5 W. For higher powers, it becomes constant under the condition of a 0.2 sccm flow rate. When the flow rate is 0.3 sccm and 0.5 sccm, the trend is similar, but the inflection points occur at lower power (∼3.5 W at 0.3 sccm; ∼2.8 W at 0.5 sccm). The peak values increase with increasing flow rate. This can be explained using the saturation effect supported by the two-dimensional distributions in the discharge chamber. The assumed two-dimensional distribution can be found in appendix D, according to the measurement and particle-in-cell simulation results in the same ECR source [49, 59]. From equation (17), we know that the saturation electron density is $\sim 2.2 \times 10^{11}$ cm^{-3} in the resonance region. This agrees with the values above 9 W at 0.5 sccm seen in figure 4(a). In these discharge conditions, the distribution of the electron density is flat, i.e. the values in the center position are close to those in the resonance position. With decreasing flow rate,

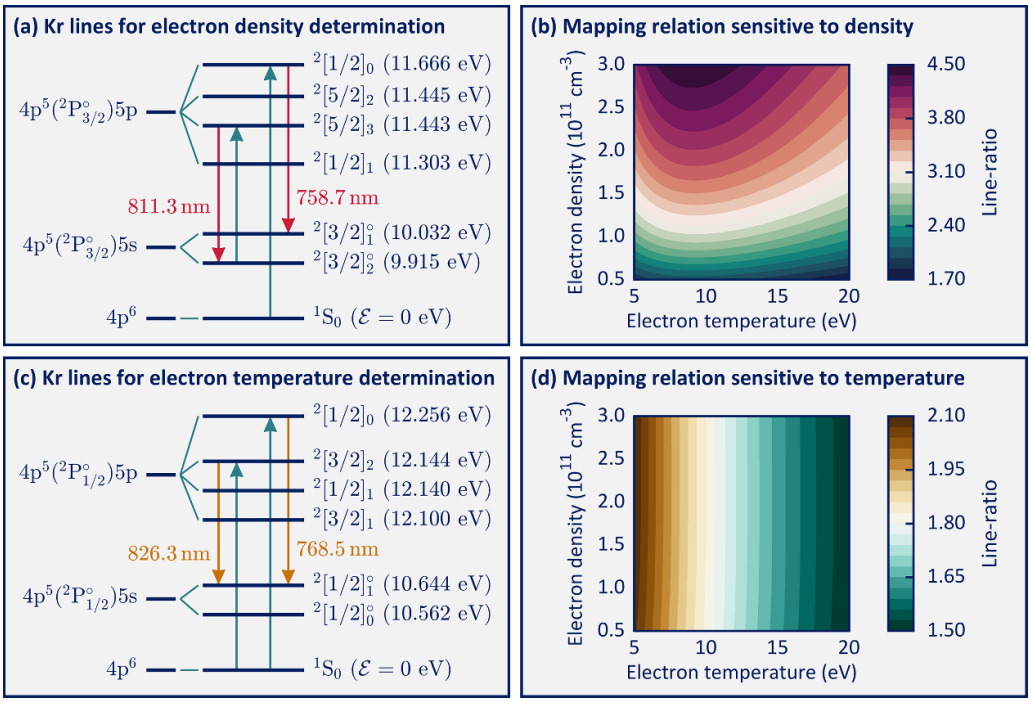

Figure 3. Collisional-radiative mechanisms and mapping relations of the Kr lines used to determine the electron density (811.3 nm/758.7 nm) and temperature (826.3 nm/768.5 nm).

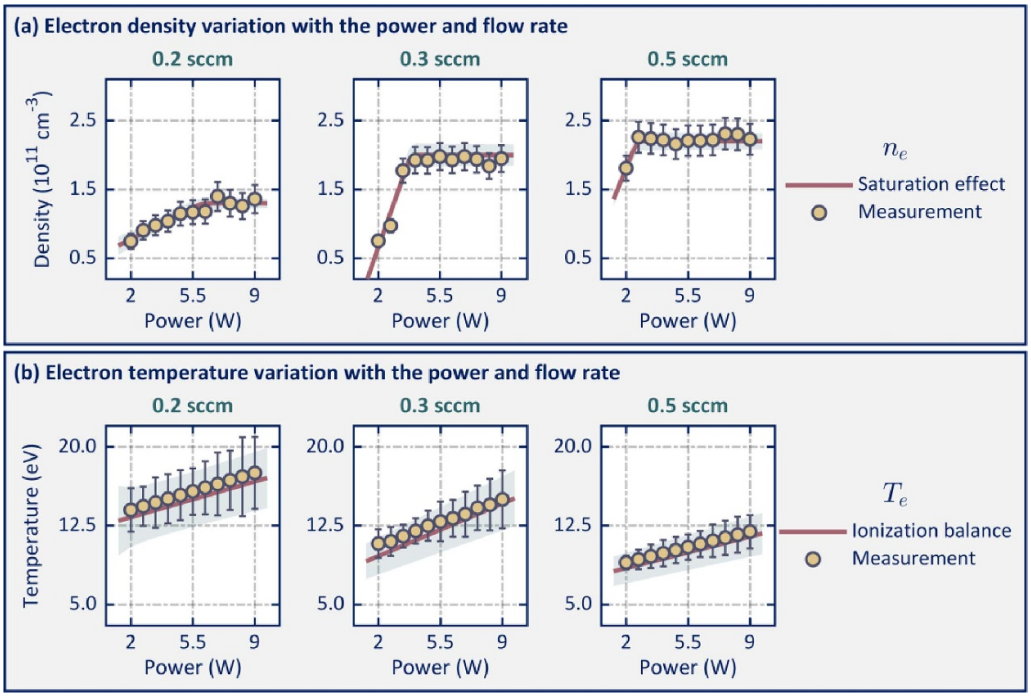

Figure 4. Electron density and temperature, obtained by the line-ratios method, versus the power at 0.2, 0.3, and 0.5 sccm molecular nitrogen flow rates.

the distribution of the electron density gradually changes from flat to steep (affected by δ in table D1), meaning that the difference in the electron density between the resonance position and center position becomes more significant. This can be used to explain why the measured saturation values become smaller with decreasing flow rates. The uncertainty in the saturation values used to verify the electron density is estimated at ∼5%–7%, while that for the measured electron density is estimated at ∼10%. Note that the uncertainty in figure 4(a) has been multiplied by 1.5 for better visibility.

Figure 4(b) shows that the electron temperature increased as the power at the flow rate of 0.2, 0.3 and 0.5 sccm, but the

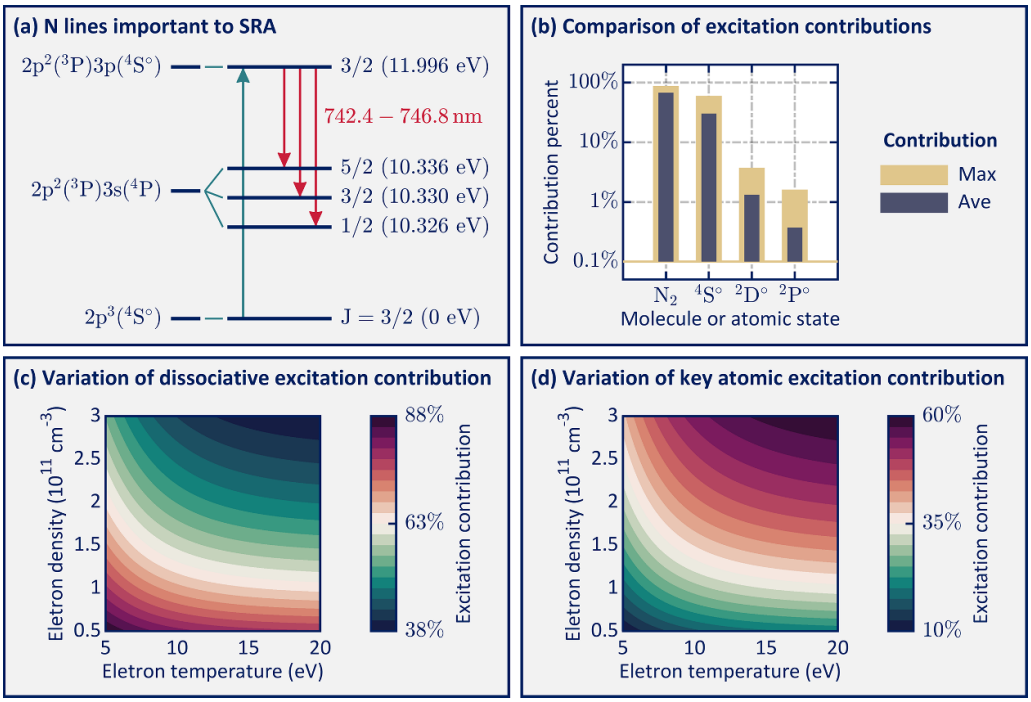

Figure 5. Kinetics of the N($2p^2(^3P)3p\ ^4S°$) state. (a) N lines important to SRA; (b) comparison of excitation contributions to the N($2p^2(^3P)3p\ ^4S°$) state; (c) and (d) variation of the contributions from molecular dissociative excitation and the excitation from the ground state as a function of electron density and temperature, respectively.

electron temperature decreases as the increment of the flow rate (from the 0.2–0.5 sccm) The phenomenon that the electron temperature increases with the power can be understood from the evolution of the plasma potential observed in [60], in which the gradient of the plasma potential increases with the power, causing the electrons to transition from the resonance position to the center position. In addition, the uncertainty measured by the line-ratio method is ∼10%–20%, due to the residual error associated with the line-ratio fitting. The uncertainty of the ionization balance model is ∼15%–25%. It consists of three uncertainties: (a) the uncertainty caused by the edge-to-center ratio h_l and h_R, ∼5%–20% [61]; (b) the uncertainty of the ionization cross section of molecular nitrogen, ∼5% recommended by Itikawa [50]; (c) the uncertainty of the N_2 ion percentage in the plasma (χ in table C1), ∼15%.

The trend of the electron temperature and density versus the power and flow rate by the Langmuir probes in the similar ECR plasma source using xenon gas is the same as our results, and the order of magnitude is also close to our results [58]. The maximum value of the electron temperature is ∼15 eV with the xenon gas, and ∼18 eV in our measurement with N_2/Kr gas. The maximum value of the electron density is $\sim 2.2 \times 10^{11}\ cm^{-3}$ both with the xenon and N_2/Kr working gases, which has been explained by the saturation effect in [49].

4.3. Kinetics of the $2p^2(^3P)3p\ ^4S°$, $2p^2(^3P)3p\ ^2D°$, and $2p^2(^3P)3p\ ^2P°$ states of atomic nitrogen

Figures 5(a) and (b) show the kinetics between the N($2p^3\ ^4S°$) and N($2p^2(^3P)3p\ ^4S°$) states and the comparison of excitation contributions to the N($2p^2(^3P)3p\ ^4S°$) state. It can be seen that the population of the N($2p^2(^3P)3p\ ^4S°$) state is governed by dissociative excitation of molecular nitrogen and ground-state excitation. Figures 5(c) and (d) show the percentage of the contribution of dissociative excitation and atomic excitation from the N($2p^3\ ^4S°$) state. At low electron density and temperature ($5 \times 10^{10}\ cm^{-3}$ and 5 eV), the population of the N($2p^2(^3P)3p\ ^4S°$) state is dominated by dissociative excitation (∼88%), but when the electron density and temperature increase, atomic excitation becomes important (∼30% at $10^{11}\ cm^{-3}$ and 10 eV). In addition, figure 3(a) shows that the Kr($4p^5(^2P°_{3/2})5p\ ^2[1/2]_0$) state is predominantly populated by electron-impact excitation from the ground state. Therefore, the density of N($2p^3\ ^4S°$) states indeed has a functional relationship to the emission lines from the N($2p^2(^3P)3p\ ^4S°$) and Kr($4p^5(^2P°_{3/2})5p\ ^2[1/2]_0$) states, as shown in equation (10) of table 5.

Figures 6(a) and (b) show the kinetics between the N($2p^3\ ^2D°$) and N($2p^2(^3P)3p\ ^2D°$) states and the comparison of excitation contributions to the N($2p^2(^3P)\ 3p\ ^2D°$) state. It can be seen that the population of the N($2p^2(^3P)3p\ ^2D°$) state is governed by dissociative excitation of molecular nitrogen and atomic excitation from the N($2p^3\ ^2D°$) state. Figures 6(c) and (d) show the percentage of the contribution of dissociative and atomic excitation. At low electron density and temperature ($5 \times 10^{10}\ cm^{-3}$ and 5 eV), the population of N($2p^2(^3P)3p\ ^2D°$) is dominated by dissociative excitation (∼93%). However, when the electron density and temperature increase, atomic excitation becomes important, growing to ∼10% at $10^{11}\ cm^{-3}$ and 10 eV. Therefore, similar to the case of N($2p^3\ ^4S°$), the density of N($2p^3\ ^2D°$) has a functional

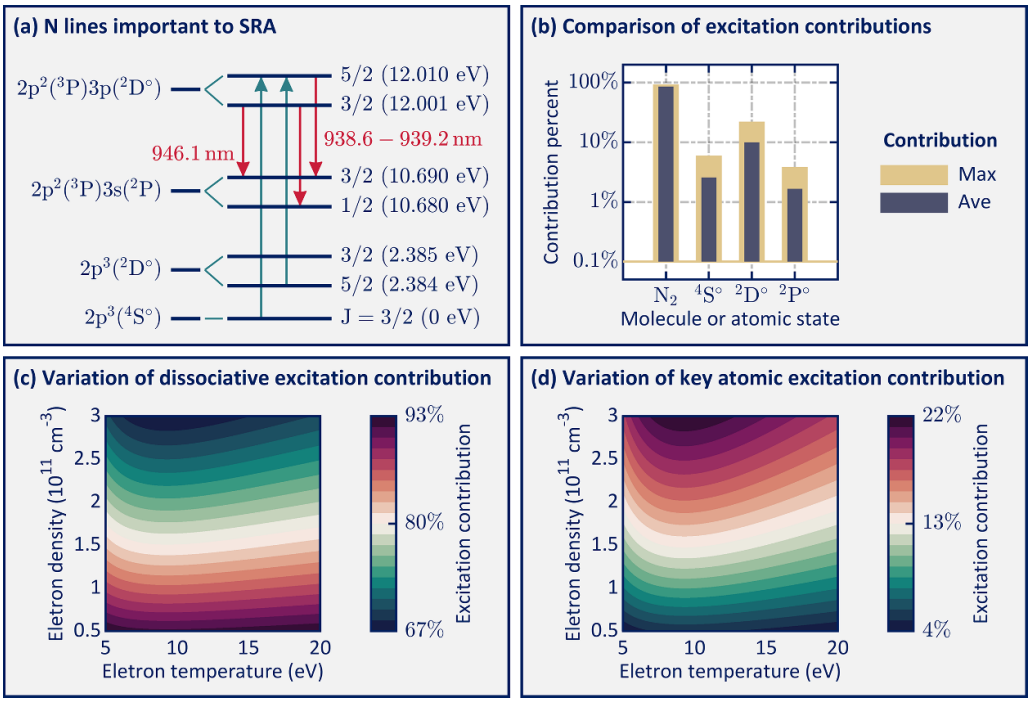

Figure 6. Kinetics of the N($2p^2(^3P)3p\ ^2D^\circ$) state. (a) N lines important to SRA; (b) comparison of excitation contributions to the N($2p^2(^3P)3p\ ^2D^\circ$) state; (c) and (d) variation of the contributions from molecular dissociative excitation and excitation from the intra-shell excited state ($2p^3\ ^2D^\circ$) as a function of electron density and temperature, respectively.

relationship to the emission lines from the N($2p^2(^3P)3p\ ^2D^\circ$) and Kr($4p^5(^2P^\circ_{3/2})5p\ ^2[1/2]_0$) states, as shown in equation (10) of table 5.

Figures 7(a) and (b) show the kinetics between the N($2p^3\ ^2P^\circ$) and N($2p^2(^3P)3p\ ^2P^\circ$) state and the comparison of excitation contributions to the N($2p^2(^3P)3p\ ^2P^\circ$) state. It can be seen that the population of the N($2p^2(^3P)3p\ ^2P^\circ$) state is governed by dissociative excitation of molecular nitrogen and excitation from intra-shell excited states. Figures 7(c) and (d) show the percentage of the contributions from dissociative excitation and atomic excitation from the N($2p^3\ ^2P^\circ$) state. At low electron density and temperature (5×10^{10} cm^{-3} and 5 eV), the population of N($2p^2(^3P)3p\ ^2P^\circ$) is dominated by dissociative excitation (∼91%). However, when the electron density and temperature increase, atomic excitation becomes important, growing to ∼12% at 10^{11} cm^{-3} and 10 eV. Therefore, similar to N($2p^3\ ^4S^\circ$) and N($2p^3\ ^2D^\circ$), the density of N($2p^3\ ^2P^\circ$) again has a functional relationship to the emission lines from the N ($2p^2(^3P)3p\ ^2P^\circ$) and Kr($4p^5(^2P^\circ_{3/2})5p\ ^2[1/2]_0$) states.

Figures 8(a)–(c) show the densities of atoms in the N($2p^3\ ^4S^\circ$), N($2p^3\ ^2D^\circ$), and N($2p^3\ ^2P^\circ$) states versus the power and flow. Their densities are determined by equations (10)–(13) in table 5, where T_e is obtained by the line-ratio of Kr (826.3 nm/768.5 nm). From figure 8(a), it is seen that the N($2p^3\ ^4S^\circ$) densities rise with the power and flow, and the peak value occurs under the conditions of 0.5 sccm and 9 W. The trends in N($2p^3\ ^2D^\circ$) and N($2p^3\ ^2P^\circ$) are similar to N($2p^3\ ^4S^\circ$), but the densities of N($2p^3\ ^4S^\circ$) are about twice those of N($2p^3\ ^2D^\circ$), i.e. one order of magnitude larger than those of N($2p^3\ ^2P^\circ$). The measured densities are compared with those obtained from the dissociation model. It is seen that the agreement between the two methods is quite good at high power values (>3 W) within the given uncertainty. However, there are minor discrepancies for N($2p^3\ ^2D^\circ$) and N($2p^3\ ^2P^\circ$) at lower power values, due to the kinetics of N($2p^2(^3P)3p\ ^2D^\circ$) and N($2p^2(^3P)3p\ ^2D^\circ$) being dominated by dissociative excitation at low electron densities, as shown in figures 6 and 7. At the flow rate of 0.2 sccm, only a few measured points are shown because the spectrometer used in our work has a weak quantum conversion efficiency for wavelengths larger than 900 nm. Note that the uncertainties of the measured N($2p^3\ ^4S^\circ$) and N($2p^3\ ^2D^\circ$) densities at 0.2 sccm are magnified by a factor of 1.5 in figures 8(a) and (c) for better visibility. The uncertainty of the dissociation model is estimated at ∼30% in figures 8(a)–(c). It is mainly due to the branching ratio of the total dissociation cross section. In our work, we assumed a constant branching ratio to yield the N($2p^3\ ^2D^\circ$) and N($2p^3\ ^2P^\circ$) cross sections, but in reality the branching is a function of the electron energy. The uncertainty of the SRA method will be discussed in section 5.2.

5. Discussion

We now present a novel concept, the ‘excited-state system’, which can serve as a guide to building a diagnostic method for determining the number densities of the occupied states of interest. The method for determining which certain states included in the excited-state system is based on

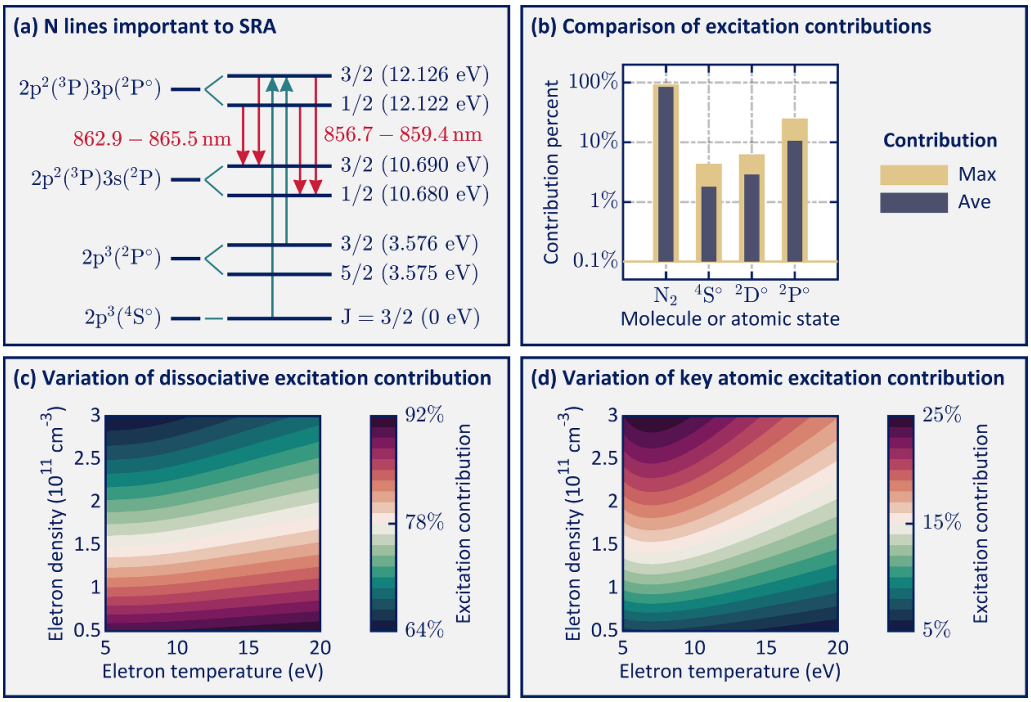

Figure 7. Kinetics of the N($2p^2(^3P)3p\ ^2P°$) state. (a) N lines important to SRA; (b) comparison of excitation contributions to the N($2p^2(^3P)3p\ ^2P°$) state; (c) and (d) variation of the contributions from molecular dissociative excitation and excitation from the intra-shell excited state ($2p^3\ ^2P°$) as a function of electron density and temperature, respectively.

some important propensity and selection rules considering the quantum numbers of the states involved. In addition, we evaluate possible uncertainties in the SRA method. At last, we discuss the applicability range of the state-resolved method.

5.1. Excited-state system and propensity/selection rules for optical diagnostics

An excited-state system is defined as a nearly closed excitation–deexcitation cyclic system between a few selected states. Being essentially independent from the other states, one can find emission lines that are sensitive to the parameters of interest among the many emission lines observed in generally very complex experimental spectra. Below, we summarize propensity rules based on the quantum numbers of the states involved. These rules serve as a guide for selecting the particular states included in the system.

This concept is ideally suited for our method of determining the number densities of atomic nitrogen states. Three excited-state systems are presented in table 7, namely the 'N($2p^3\ ^4S°$) excited-state system', the 'N($2p^3\ ^2D°$) excited-state system', and the 'N($2p^3\ ^2P°$) excited-state system'. In the case of atomic nitrogen, each excited-state system includes three states, i.e. the ground state or an intra-shell excited state, a 3s intermediate state, and a 3p excited state. The states included in the excited-state systems have the following properties: (i) the lowest state is the ground state or an intra-shell excited metastable state; (ii) the emitting states decay to the lowest state by one or more optical transitions (in the case of atomic nitrogen, two optical transitions from an emitting 3p state lead to the lowest state via an intermediate 3s state); (iii) the electron-impact excitation cross section for the transition from the lowest state to the emitting state must be large compared to other electron-driven transitions that might populate the emitting state.

The above criteria can be explained by using propensity/selection rules involving the relevant quantum numbers. The ground-state and the intra-shell excited states have a significant density compared to that of other states in most discharges. Now let us compare the electron-impact cross sections for exciting the selected emitting states from the three lowest states to verify the propensities. Specifically, except for near-threshold, spin-forbidden transitions ($\Delta S \neq 0$, as in exciting the $2p^2(^3P)3p\ ^2D°$ state from the $2p^3\ ^4S°$ state of atomic nitrogen), are generally small compared to spin-allowed but parity-forbidden transitions ($\Delta S \neq 0$ but the same parity, as in exciting the $2p^2(^3P)3p\ ^4S°$ state from the $2p^3\ ^4S°$ state or the $2p^2(^3P)3p\ ^2D,P^o$ states from the $2p^3\ ^2D,P°$ states). The latter, in turn, are small compared to dipole-allowed transitions ($\Delta S = 0$; $\Delta L = 0, \pm1$; $\Delta J = 0, \pm1$; opposite parity between the initial and final states). (These dipole-allowed transitions are not relevant for our setup in nitrogen but for the other gas case, i.e. oxygen) Among the spin-allowed but dipole-forbidden transitions, the cross sections satisfying the condition $\Delta L = 0$ in atomic nitrogen tend to be larger compared to the $\Delta L = \pm1$ transitions. For example, the cross section for exciting the $2p^2(^3P)3p\ ^2D°$ state from the $2p^3\ ^2D°$ state is generally larger by about a factor of 2.7 compared to exciting the

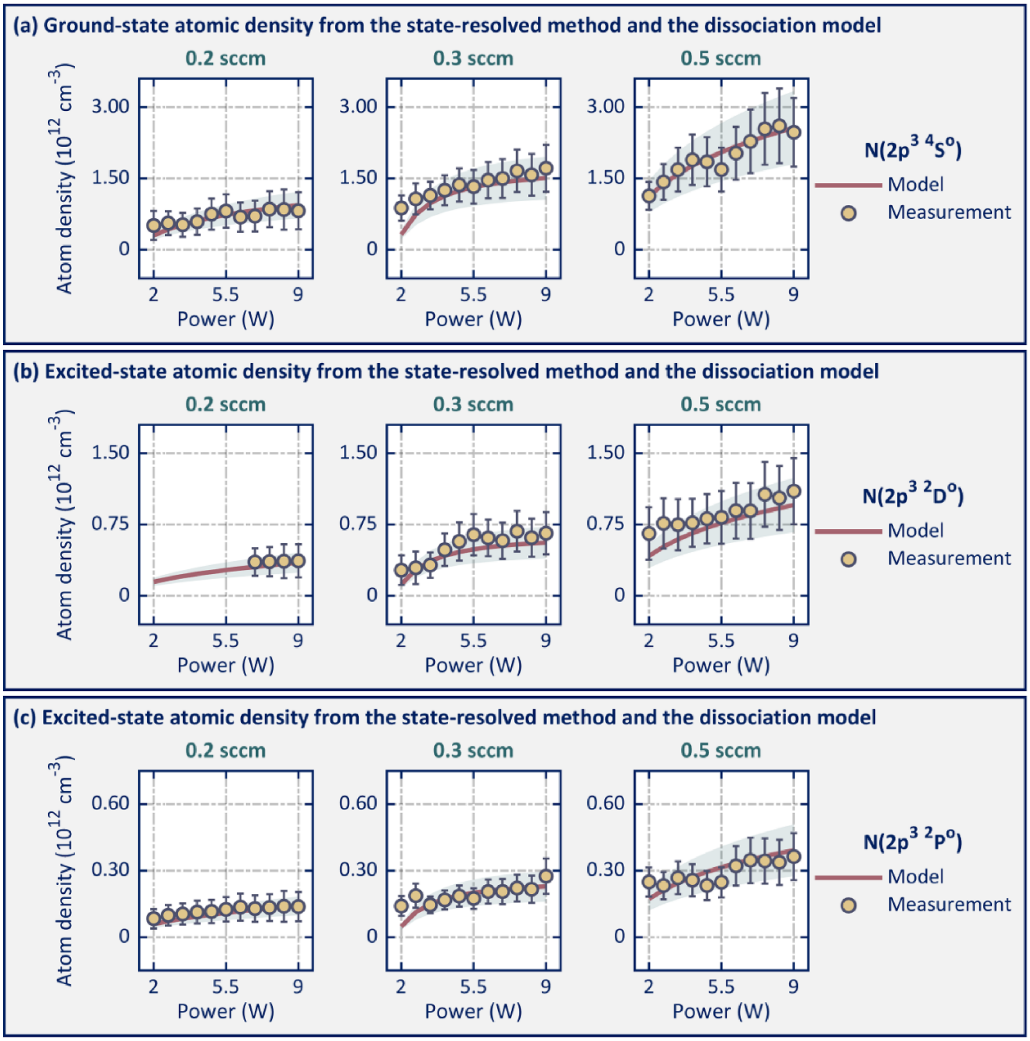

Figure 8. Number densities of atoms in the ground state as well as the intra-shell excited states, measured by our state-resolved actinometry method and calculated based on the dissociation model. (a) Density of the N(2p^3 ^{4}S°) state versus power and molecular nitrogen flow rates; (b) density of the N(2p^3 ^{2}D°) state versus power and molecular nitrogen flow rates; (c) density of the N(2p^3 ^{2}P°) state versus the power and molecular nitrogen flow rates. The scatter points in panels (a)–(c) are the measured values, while the straight lines are the calculated values.

former from the 2p^3 ^{2}P° state. Our particular choices have been confirmed by *ab initio* BSR calculations and, in a few cases, also by experiment. These properties of the cross sections, which lead to the kinetics relations displayed in figures 5–7, are a helpful guide in choosing the certain states to construct excited-state systems.

5.2. Uncertainty of the SRA method

The uncertainty of the SRA results depicted in figure 8 is evaluated in table 8. We consider the following two types: (i) the uncertainty of the coefficients (Δ_C, Δ_α and Δ_ξ) in equation (10); (ii) the uncertainty in the spectral measurement ($\Delta_{I(xi)}$).

(i) The uncertainty in the coefficients includes: (a) the actinometric coefficient uncertainty Δ_C, (b) the excitation coefficient Δ_α, and (c) the fractional actinometer uncertainty Δ_ξ. (a) Δ_C can be determined from the residual error associated with the line-ratio fitting (∼5%–12%) and the uncertainties of the cross sections involved (∼10% for electron-impact excitations in nitrogen, also 10% for excitations in krypton). The reason for considering the residual error of the line ratio is that the rate coefficients in Δ_C are affected by the electron temperature T_e, as shown in equation (10). Also, T_e is obtained by the line-ratio method. It is worth noting that the uncertainty of the original cross section for the excitation process, e + Kr(4p^6 ^{1}S$_0$) → e + Kr(4p^5(^{2}P°$_{3/2}$)5p ^{2}[1/2]$_0$), is ∼13%–20%. Since this is significant for the measurement, we revised the data by comparing the model's line ratios (811.3 nm/758.7 nm) with those from the experiment. (b) The method of estimating Δ_α is similar to that of Δ_C; the difference is that Δ_α is affected by the cross sections of both dissociative excitation (∼15%) and atomic excitation

Table 7. Excited-state systems for measuring state-resolved atomic nitrogen densities.

$N(2p^3\,{}^4S^\circ)$ excited-state system										
Emitting state			Intermediate state			Lower state			λ (nm)	
Conf.	Term	J	Conf.	Term	J	Conf.	Term	J	Former	Latter
$2s^22p^2(^3P)3p$	$^4S^\circ$	3/2	$2s^22p^2(^3P)3\,s$	^4P	1/2	$2s^22p^3$	$^4S^\circ$	3/2	742.36	120.07
$2s^22p^2(^3P)3p$	$^4S^\circ$	3/2	$2s^22p^2(^3P)3\,s$	^4P	3/2	$2s^22p^3$	$^4S^\circ$	3/2	744.23	120.02
$2s^22p^2(^3P)3p$	$^4S^\circ$	3/2	$2s^22p^2(^3P)3\,s$	^4P	5/2	$2s^22p^3$	$^4S^\circ$	3/2	756.83	119.95
$N(2p^3\,{}^2D^\circ)$ excited-state system										
Emitting state			Intermediate state			Lower state			λ(nm)	
Configuration	Term	J	Configuration	Term	J	Configuration	Term	J	former	latter
$2s^22p^2(^3P)3p$	$^2D^\circ$	3/2	$2s^22p^2(^3P)3\,s$	^2P	1/2	$2s^22p^3$	$^2D^\circ$	3/2	938.68	149.46
$2s^22p^2(^3P)3p$	$^2D^\circ$	5/2	$2s^22p^2(^3P)3\,s$	^2P	3/2	$2s^22p^3$	$^2D^\circ$	3/2	939.28	149.28
$2s^22p^2(^3P)3p$	$^2D^\circ$	3/2	$2s^22p^2(^3P)3\,s$	^2P	3/2	$2s^22p^3$	$^2D^\circ$	5/2	946.07	149.26
$N(2p^3\,{}^2P^\circ)$ excited-state system										
Emitting state			Intermediate state			Lower state			λ (nm)	
Configuration	Term	J	Configuration	Term	J	Configuration	Term	J	Former	Latter
$2s^22p^2(^3P)3p$	$^2P^\circ$	3/2	$2s^22p^2(^3P)3s$	^2P	1/2	$2s^22p^3$	$^2P^\circ$	1/2	856.77	174.52
$2s^22p^2(^3P)3p$	$^2P^\circ$	1/2	$2s^22p^2(^3P)3s$	^2P	1/2	$2s^22p^3$	$^2P^\circ$	3/2	859.40	17.53
$2s^22p^2(^3P)3p$	$^2P^\circ$	3/2	$2s^22p^2(^3P)3s$	^2P	3/2	$2s^22p^3$	$^2P^\circ$	1/2	862.92	174.27
$2s^22p^2(^3P)3p$	$^2P^\circ$	1/2	$2s^22p^2(^3P)3s$	^2P	3/2	$2s^22p^3$	$^2P^\circ$	3/2	865.59	147.27

(∼10%). (c) The uncertainty Δ_ξ is ∼3% at low flow rate (q) and input power ($P_{\rm in}$), while it grows to ∼10% at high q and $P_{\rm in}$, considering the variation in the dissociation ratio of molecular nitrogen.

(ii) The uncertainty in the spectral measurement can be determined from the noise-to-signal ratio of emission lines. The experimental data show that noise affects the emission lines from $N(2p^2(^3P)3p\ ^2D^\circ)$ most significantly. For instance, the 938.60 nm and 939.2 nm line's noise-to-signal is ∼12%–50%, while the noise-to-signal ratio for those from $N(2p^2(^3P)3p\ ^2P^\circ)$ is ∼2%–20%.

Besides the above two types of uncertainty listed in table 8, the uncertainty induced by equation (10) is also considered. It can be estimated from the percentage contribution of atomic excitation $\eta_{\rm exc(}{}_{xi)}$, typically ∼7%. Note that $\Delta_{\eta{\rm exc(}xi)}$ is not listed in table 8, because it is much smaller than the coefficient and experiment uncertainty. However, the total uncertainty includes $\Delta_{\eta{\rm exc(}xi)}$, which is listed in table 8 under the representative operating conditions.

5.3. Applicability range of the SRA method

The premise of our method is that the ground state and intra-shell excited states contribute to the corresponding emission states, typically with $\eta_{\rm exc(}{}_{xi)} > 10\%$, as shown in figures 5–7. Thus, the approach is applicable in a specific range, namely when $n_{\rm e}$ is larger than 10^{11} cm^{-3}, resulting in the dissociation degree of the plasma source being >1%. The dissociation degree condition can not only be satisfied in ECR plasma (∼0.1–1 Pa), but also in higher pressure, such as in ICP plasma (∼2.6 Pa and 26 Pa), microwave micro-plasma (300 Pa), and glide arc plasma (atmospheric pressure) [29, 62–64]. Within the above range, our method has an acceptable uncertainty ($\Delta yi\ n < 30\%$). But, it is worth noting that the loss of the emitting states is governed by the quenching processes instead of the radiation processes in higher pressure, especially the atmospheric pressure. Hence, the actinometry equation needs to consider the quenching processes. In addition, the noise-to-signal ratio affects the uncertainty. As shown in figure 7(a), the $N(2p^2(^3P)3p\ ^2D^\circ)$ emission lines with wavelengths of 938.6 nm, 939.2 nm, and 946.1 nm, respectively, are weak in the experiment. This is due to the low quantum efficiency (QE < 0.2) of our detectors when the wavelength is larger than 900 nm, thereby causing a significant uncertainty. Therefore, the performance of the spectrometer needs to be considered in the measurement.

In summary, our method is suitable for plasma sources with relatively high dissociative degree, corresponding to significant contributions of atomic excitation to populate the emitting atomic states. Moreover, to decrease the experimental uncertainty, one must consider the quantum efficiency of the detectors in the desired wavelength range.

Table 8. Total uncertainty Δ_n^{yi} of the SRA method, including the uncertainties of the actinometric coefficient Δ_C, the excitation coefficient Δ_α, the fractional actinometer in the gas (Δ_ξ), and the actinometric signal $\Delta_{I(xi)}$ introduced in equations (10)–(13). Here, *xi* refers to the excited states of atomic nitrogen ($x = 1, 2, 3$) corresponds to $N(2p^2(^3P)3p\ ^4S^\circ)$, $N(2p^2(^3P)3p\ ^2D^\circ)$, and $N(2p^2(^3P)3p\ ^2P^\circ)$, while *yi* refers to the measured atoms ($i = 1, 2, 3$) corresponds to $N(2p^3\ ^4S^\circ)$, $N(2p^3\ ^2D^\circ)$, and $N(2p^3\ ^2P^\circ)$.

Condition		Coefficient uncertainty			Experimental uncertainty			Total uncertainty		
q	P_{in}	Δ_C	Δ_α	Δ_ξ	$\Delta_{I(x1)}$	$\Delta_{I(x2)}$	$\Delta_{I(x3)}$	$\Delta y1\ n$	$\Delta y2\ n$	$\Delta y3\ n$
0.2	2.1	14.1	18.9	2.95	31.1	\	23.9	39.97	\	34.88
	2.8	13.4	18.4	4.21	17.2	\	20.0	29.79	\	31.83
	3.5	14.7	19.4	5.17	18.2	\	15.5	31.70	\	30.58
	7.0	19.2	20.2	8.07	6.70	26.4	6.98	30.61	40.12	30.99
	9.0	20.0	20.8	9.14	5.73	35.1	6.40	31.61	47.11	32.06
0.3	2.1	11.6	18.3	2.09	19.2	53.0	21.1	30.05	57.99	31.60
	2.8	13.9	18.3	4.83	18.2	52.0	14.8	30.64	57.72	29.07
	3.5	13.4	18.0	6.38	6.89	33.1	6.96	25.30	41.28	25.59
	7.0	15.0	19.2	9.20	3.54	18.4	3.73	27.18	32.84	27.43
	9.0	16.4	20.3	9.78	3.12	17.1	2.87	28.89	33.64	29.09
0.5	2.1	13.5	18.5	4.40	9.31	34.3	9.61	26.07	42.23	26.40
	2.8	14.5	19.3	5.41	5.93	23.3	5.83	26.35	34.83	26.49
	3.5	15.4	19.9	6.22	4.87	23.8	4.81	27.25	36.01	27.40
	7.0	16.8	21.1	8.91	2.19	14.8	2.67	29.31	32.93	29.50
	9.0	16.4	20.7	9.90	1.92	12.1	2.03	29.10	31.63	29.26

6. Conclusions

In the present work, we have proposed a novel SRA method to measure the densities of $N(2p^3\ ^4S^\circ)$, $N(2p^3\ ^2D^\circ)$, and $N(2p^3\ ^2P^\circ)$ in a nitrogen-containing krypton ECR plasma, based on the kinetic investigation of the ground state and intra-shell excited states. The measured densities were compared with those calculated by the dissociation model, and they are generally found to be in good agreement. Furthermore, we presented a Kr line-ratio method to determine the electron density and temperature, based on the kinetics of the Kr(5p) states. The measured electron density and temperature were verified with the saturation effect of the ECR plasma and the ionization model, respectively. A novel concept, the 'excited-state system', was introduced to help finding particular states that are sensitive to the measured parameters, based on an analysis of general quantum number propensity/selection rules. Hence, it is possible to extend our method to measure other particles' densities using the concept for guidance. The uncertainty and the applicability range of our method were also discussed to consider the validity of our method. We plan to employ the SRA method presented here to other number-density measurements in future work.

Data availability statement

All the data that support the findings of this study are included within this article and any supplementary files.

Acknowledgments

The authors would like to express their gratitude to Mr Quan Jin and Mr Sheng-Feng Meng for their help with the experiment and design of the plasma source. This work is financially supported by the National Natural Science Foundation of China under Grant No. U22B2094, the National Key R&D Program of China under Grant No. 2020YFC2201000, and the Fundamental Research Funds for the Central Universities No. 2023FRFK06006. The work of K B is supported by the United States National Science Foundation under Grant Nos. PHY-1834740 and PHY-2110023.

Appendix

This appendix lists the reaction sets for the nitrogen plasma (table A1 in appendix A) and the krypton plasma (tables B1 and B2 in appendix B) considered in the CR model, as well as the equations considered in the ionization balance model (table C1 in appendix C) and the two-dimensional distribution of the plasma parameters (table D1 in appendix D).

Appendix A. Reaction set for the nitrogen plasma

Appendix A includes the complete nitrogen plasma reaction set used in our CR model. The rate coefficients for these reaction sets can be found in the supplementary material.

Table A1. Reaction set for the nitrogen plasma, involving the atomic states considered in table 2 and the nitrogen molecular and atomic ions.

	Reactions	References
Electron-impact ionization processes		
A_1	$e + N_2 \rightarrow e + N_2^+$	[50, 51]
A_2	$e + N(^4S^\circ, {}^2D^\circ, {}^2P^\circ) \rightarrow e + N^+$	[40]
Electron-impact dissociation and dissociation-excitation processes		
A_3	$e + N_2 \rightarrow e + N(^4S^\circ) + N(^4S^\circ, {}^2D^\circ, {}^2P^\circ)$	[40]
A_4	$e + N_2 \rightarrow e + N(^4S^\circ) + N(3sx)$	[65]
A_5	$e + N_2 \rightarrow e + N(^4S^\circ) + N(3px)$	[65]
Electron-impact atomic excitation processes		
A_6	$e + N(^4S^\circ) \leftrightarrow e + N(^2D^\circ, {}^2P^\circ)$	[40]
A_7	$e + N(^2D^\circ) \leftrightarrow e + N(^2P^\circ)$	[40]
A_8	$e + N(^4S^\circ) \leftrightarrow e + N(3sx)$	[40]
A_9	$e + N(^2D^\circ) \leftrightarrow e + N(3sx)$	[40]
A_{10}	$e + N(^2P^\circ) \leftrightarrow e + N(3sx)$	[40]
A_{11}	$e + N(3sy) \leftrightarrow e + N(3sx)$	[40]
A_{12}	$e + N(^4S^\circ) \leftrightarrow e + N(3px)$	[40]
A_{13}	$e + N(^2D^\circ) \leftrightarrow e + N(3px)$	[40]
A_{14}	$e + N(^2P^\circ) \leftrightarrow e + N(3px)$	[40]
A_{15}	$e + N(3py) \leftrightarrow e + N(3px)$	[40]
Diffusion processes		
A_{16}	$N(^4S^\circ) \rightarrow 1/2N_2$	[42–44]
A_{17}	$N(^2D^\circ, {}^2P^\circ) \rightarrow N(^4S^\circ)$	[43, 45]
A_{18}	$N(3si) \rightarrow N(^4S^\circ)$	[43, 45]
A_{19}	$N(3pi) \rightarrow N(^4S^\circ)$	[43, 45]
A_{20}	$N^+ \rightarrow N_2$	
A_{21}	$N^+ \rightarrow N(^4S^\circ)$	
Radiation processes		
A_{22}	$N\ (3s\ {}^4P) \rightarrow N\ (^4S^\circ) + hv$	[41]
A_{23}	$N\ (3s\ {}^2P) \rightarrow N\ (^2D^\circ) + hv$	[41]
A_{24}	$N\ (3s\ {}^2P) \rightarrow N\ (^2P^\circ) + hv$	[41]
A_{25}	$N\ (2p^4\ {}^4P) \rightarrow N\ (^4S^\circ) + hv$	[41]
A_{26}	$N\ (3p\ {}^2S^\circ) \rightarrow N\ (3\ s\ {}^2P) + hv$	[41]
A_{27}	$N\ (3p\ {}^4D^\circ) \rightarrow N\ (3\ s\ {}^4P) + hv$	[41]
A_{28}	$N\ (3p\ {}^4S^\circ) \rightarrow N\ (3\ s\ {}^4P) + hv$	[41]
A_{29}	$N\ (3p\ {}^4P^\circ) \rightarrow N\ (3s\ {}^4P) + hv$	[41]
A_{30}	$N\ (3p\ {}^2P^\circ) \rightarrow N\ (3s\ {}^2P) + hv$	[41]
A_{31}	$N\ (3p\ {}^2D^\circ) \rightarrow N\ (3s\ {}^2P) + hv$	[41]

Appendix B. Reaction set for the krypton plasma

Tables B1 and B2 list the states and reaction sets used in our krypton plasma CR model. The rate coefficients of these reaction sets can be found in the supplementary material.

Table B1. Kr states in the present CR model.

	State	Term	J	E (eV)	Symbol
1	$4s^2 4p^6$	^{1}S	0	0	Kr(gs)
2	$4s^2 4p^5(^2\mathrm{P}^\circ_{3/2})5s$	^{2}[3/2]°	2	9.915	Kr($1s_5$)
3	$4s^2 4p^5(^2\mathrm{P}^\circ_{3/2})5s$	^{2}[3/2]°	1	10.032	Kr($1s_4$)
4	$4s^2 4p^5(^2\mathrm{P}^\circ_{3/2})5s$	^{2}[1/2]°	0	10.562	Kr($1s_3$)
5	$4s^2 4p^5(^2\mathrm{P}^\circ_{3/2})5s$	^{2}[1/2]°	1	10.644	Kr($1s_2$)
6	$4s^2 4p^5(^2\mathrm{P}^\circ_{3/2})5p$	^{2}[1/2]	1	11.303	Kr($2p_{10}$)
7	$4s^2 4p^5(^2\mathrm{P}^\circ_{3/2})5p$	^{2}[5/2]	3	11.443	Kr($2p_9$)
8	$4s^2 4p^5(^2\mathrm{P}^\circ_{3/2})5p$	^{2}[5/2]	2	11.444	Kr($2p_8$)
9	$4s^2 4p^5(^2\mathrm{P}^\circ_{3/2})5p$	^{2}[3/2]	1	11.526	Kr($2p_7$)
10	$4s^2 4p^5(^2\mathrm{P}^\circ_{3/2})5p$	^{2}[3/2]	2	11.546	Kr($2p_6$)
11	$4s^2 4p^5(^2\mathrm{P}^\circ_{3/2})5p$	^{2}[1/2]	0	11.666	Kr($2p_5$)
12	$4s^2 4p^5(^2\mathrm{P}^\circ_{1/2})5p$	^{2}[3/2]	1	12.100	Kr($2p_4$)
13	$4s^2 4p^5(^2\mathrm{P}^\circ_{1/2})5p$	^{2}[1/2]	1	12.125	Kr($2p_3$)
14	$4s^2 4p^5(^2\mathrm{P}^\circ_{1/2})5p$	^{2}[3/2]	2	12.140	Kr($2p_2$)
15	$4s^2 4p^5(^2\mathrm{P}^\circ_{1/2})5p$	^{2}[1/2]	0	12.256	Kr($2p_1$)

Table B2. The reaction set for the nitrogen plasma, involving the atomic states considered in table B2 and the nitrogen molecular and atomic ions.

	Reactions	References
Electron-impact ionization processes		
B_1	$e + Kr(gs) \rightarrow e + Kr^+$	[66]
Electron-impact atomic excitation processes		
B_2	$e + Kr(gs) \leftrightarrow e + Kr(1sx)$	[46, 47]
B_3	$e + Kr(1sy) \leftrightarrow e + Kr(1sx)$	[47]
B_4	$e + Kr(gs) \leftrightarrow e + Kr(2px)$	[47]
B_5	$e + Kr(1sy) \leftrightarrow e + Kr(2px)$	[47]
B_6	$e + Kr(2px) \leftrightarrow e + Kr(2py)$	[47]
Diffusion processes		
B_7	$Kr(1sx) \rightarrow Kr(gs)$	[48]
B_8	$Kr(2px) \rightarrow Kr(gs)$	[48]
B_9	$Kr^+ \rightarrow Kr(gs)$	
Radiation processes		
B_{10}	$Kr(1s_4) \rightarrow Kr(gs) + hv$	[41]
B_{11}	$Kr(1s_2) \rightarrow Kr(gs) + hv$	[41]
B_{12}	$Kr(2p_{10}) \rightarrow Kr(1s_5) + hv$	[41]
B_{13}	$Kr(2p_{10}) \rightarrow Kr(1s_4) + hv$	[41]
B_{14}	$Kr(2p_{10}) \rightarrow Kr(1s_3) + hv$	[41]
B_{15}	$Kr(2p_{10}) \rightarrow Kr(1s_2) + hv$	[41]
B_{16}	$Kr(2p_9) \rightarrow Kr(1s_5) + hv$	[41]
B_{17}	$Kr(2p_8) \rightarrow Kr(1s_5) + hv$	[41]
B_{18}	$Kr(2p_8) \rightarrow Kr(1s_4) + hv$	[41]
B_{19}	$Kr(2p_8) \rightarrow Kr(1s_2) + hv$	[41]
B_{20}	$Kr(2p_7) \rightarrow Kr(1s_5) + hv$	[41]
B_{21}	$Kr(2p_7) \rightarrow Kr(1s_4) + hv$	[41]
B_{22}	$Kr(2p_7) \rightarrow Kr(1s_3) + hv$	[41]
B_{23}	$Kr(2p_7) \rightarrow Kr(1s_2) + hv$	[41]
B_{24}	$Kr(2p_6) \rightarrow Kr(1s_5) + hv$	[41]
B_{25}	$Kr(2p_6) \rightarrow Kr(1s_4) + hv$	[41]
B_{26}	$Kr(2p_6) \rightarrow Kr(1s_2) + hv$	[41]
B_{27}	$Kr(2p_5) \rightarrow Kr(1s_4) + hv$	[41]
B_{28}	$Kr(2p_5) \rightarrow Kr(1s_2) + hv$	[41]
B_{29}	$Kr(2p_4) \rightarrow Kr(1s_5) + hv$	[41]
B_{30}	$Kr(2p_4) \rightarrow Kr(1s_4) + hv$	[41]
B_{31}	$Kr(2p_4) \rightarrow Kr(1s_3) + hv$	[41]
B_{32}	$Kr(2p_4) \rightarrow Kr(1s_2) + hv$	[41]
B_{33}	$Kr(2p_3) \rightarrow Kr(1s_5) + hv$	[41]
B_{34}	$Kr(2p_3) \rightarrow Kr(1s_4) + hv$	[41]
Radiation processes		
B_{35}	$Kr(2p_3) \rightarrow Kr(1s_3) + hv$	[41]
B_{36}	$Kr(2p_3) \rightarrow Kr(1s_2) + hv$	[41]
B_{37}	$Kr(2p_2) \rightarrow Kr(1s_5) + hv$	[41]
B_{37}	$Kr(2p_2) \rightarrow Kr(1s_4) + hv$	[41]
B_{39}	$Kr(2p_2) \rightarrow Kr(1s_2) + hv$	[41]
B_{40}	$Kr(2p_1) \rightarrow Kr(1s_4) + hv$	[41]
B_{41}	$Kr(2p_1) \rightarrow Kr(1s_2) + hv$	[41]

Appendix C. Ionization balance model

Table C1 lists the equations used in the ionization balance model.

Table C1. The ionization model used in this work.

	Equation	Describe
Equation (C1)	$n_{N_2^+} u_B A_{eff} = n_e n_{N_2} Q_{ion} \pi R^2 l$	$n_{N_2^+}$: density of the N_2 ions u_B: Born velocity A_{eff}: loss area of the ion n_e: electron density n_{N2}: density of N_2 Q_{ion}: the rate coefficient of the N_2 ionization process
Equation (C2)	$A_{eff} = 2\pi R^2 h_l + 2\pi R l h_R$ $h_R = 0.80(4 + \frac{R}{\lambda_i})$ $h_L = \cos(\beta z)$ $\beta = \left(\frac{\nu_{iz}}{D_{a\perp}}\right)^{1/2}, D_{a\perp} = \left(\frac{kT\nu_m}{mw_c^2}\right)^{1/2}$	R: radius of the ECR source l: axial length of the ECR source h_l: edge-to-center density ratio in the axial direction h_R: edge-to-center density ratio in the radial direction z: distance from the resonance region to the screen grid λ_i: mean free path of ion ν_{iz}: ionization frequency $\nu_{m:}$ collision frequency $w_{c:}$ electron cycle frequency
Equation (C3)	$\frac{A_{eff}}{n_{N_2} \pi R^2 l} = \chi \frac{Q_{ion}^{N_2^+}(T_e)}{u_B(T_e)}$	χ: percent of N_2 ions in plasma

Appendix D. Two-dimension distribution of the plasma parameters

Table D1 lists the assumed two-dimensional distribution of the electron density and temperature in our miniature 2 cm ECR source.

Table D1. Distribution of the electron temperature and density in the ECR discharge chamber.

	Equation	Describe
Equation (D1)	$n_e(r,z) = n_{e0}\cos(\pi \frac{z-z_0}{l})[J_0(\frac{1}{\delta(z)^2}(r-r_0))$ $+J_0(\frac{1}{\delta(z)^2}(r+r_0))]$	n_e: two-dimension profile of the electron density n_{e0}: constant electron density J_0: 0th order Bessel function δ: length scale related to the diffusion process
Equation (D2)	$T_e(r,z) = T_{e0}\cos(\pi \frac{z-z_0}{l})[J_0(\frac{1}{\delta(z)^2}(r-r_0))$ $+J_0(\frac{1}{\delta(z)^2}(r+r_0))]$	$T_{e:}$ two-dimension profile of the electron density T_{e0}: constant electron temperature r_0: radial position of the resonance z_0: axial position of the resonance l: the axial length

ORCID iDs

Xi-Ming Zhu https://orcid.org/0000-0002-6501-0096
Lu Wang https://orcid.org/0009-0003-3177-7322
Yan-Fei Wang https://orcid.org/0000-0002-9226-8279
Klaus Bartschat https://orcid.org/0000-0001-6215-5014

References

[1] Adamovich I *et al* 2022 The 2022 plasma roadmap: low-temperature plasma science and technology *J. Phys. Appl. Phys.* **55** 373001
[2] Boris D R, Johnson M J, Eddy C R and Walton S G 2022 Hollow cathode enhanced capacitively coupled plasmas in Ar/N_2/H_2 mixtures and implications for plasma enhanced *ALD J. Vac. Sci. Technol.* B **40** 044002
[3] Li H, Ishii K, Sasaki S, Kamiyama M, Oda A and Denpoh K 2023 Understanding plasma enhanced chemical vapor deposition mechanisms in tetraethoxysilane-based plasma *J. Vac. Sci. Technol.* B **41** 022208
[4] Yamashita Y, Tsukizaki R and Nishiyama K 2022 Importance of stepwise ionization from the metastable state in electron cyclotron resonance ion thrusters *J. Electr. Propuls.* **1** 2
[5] Konopliv M F, Chaplin V H, Johnson L K and Wirz R E 2023 Accuracy of using metastable state measurements in laser-induced fluorescence diagnostics of xenon ion velocity in Hall thrusters *Plasma Sources Sci. Technol.* **32** 015009
[6] Ju Y and Sun W 2015 Plasma assisted combustion: dynamics and chemistry *Prog. Energy Combust. Sci.* **48** 21–83

[7] Minesi N Q, Blanchard V P, Pannier E, Stancu G D and Laux C O 2022 Plasma-assisted combustion with nanosecond discharges. I: Discharge effects characterization in the burnt gases of a lean flame *Plasma Sources Sci. Technol.* **31** 045029

[8] Laux C O, Spence T G, Kruger C H and Zare R N 2003 Optical diagnostics of atmospheric pressure air plasmas *Plasma Sources Sci. Technol.* **12** 125–38

[9] Stancu G D 2020 Two-photon absorption laser induced fluorescence: rate and density-matrix regimes for plasma diagnostics *Plasma Sources Sci. Technol.* **29** 054001

[10] Gazeli K, Lombardi G, Aubert X, Duluard C Y, Prasanna S and Hassouni K 2021 Progresses on the use of two-photon absorption laser induced fluorescence (TALIF) diagnostics for measuring absolute atomic densities in plasmas and flames *Plasma* **4** 145–71

[11] Ono R 2016 Optical diagnostics of reactive species in atmospheric-pressure nonthermal plasma *J. Phys. D: Appl. Phys.* **49** 083001

[12] Reuter S, Sousa J S, Stancu G D and Hubertus van Helden J-P 2015 Review on VUV to MIR absorption spectroscopy of atmospheric pressure plasma jets *Plasma Sources Sci. Technol.* **24** 054001

[13] Patnaik A K, Adamovich I, Gord J R and Roy S 2017 Recent advances in ultrafast-laser-based spectroscopy and imaging for reacting plasmas and flames *Plasma Sources Sci. Technol.* **26** 103001

[14] Offerhaus B, Kogelheide F, Jalat D, Bibinov N, Schulze J, Stapelmann K and Awakowicz P 2019 Determination of NO densities in a surface dielectric barrier discharge using optical emission spectroscopy *J. Appl. Phys.* **126** 193301

[15] Donnelly V M, Malyshev M V, Schabel M, Kornblit A, Tai W, Herman I P and Fuller N C M 2002 Optical plasma emission spectroscopy of etching plasmas used in Si-based semiconductor processing *Plasma Sources Sci. Technol.* **11** A26–30

[16] Kambara M, Kawaguchi S, Lee H J, Ikuse K, Hamaguchi S, Ohmori T and Ishikawa K 2022 Science-based, data-driven developments in plasma processing for material synthesis and device-integration technologies *Jpn. J. Appl. Phys.* **62** SA0803

[17] Donnelly V M and Kornblit A 2013 Plasma etching: yesterday, today, and tomorrow *J. Vac. Sci. Technol.* A **31** 050825

[18] Sridhar S, Liu L, Hirsch E W, Donnelly V M and Economou D J 2016 Insights into the mechanism of in-plasma photo-assisted etching using optical emission spectroscopy *J. Vac. Sci. Technol.* A **34** 061303

[19] Arora P, Cho J, Cervantes R and Donnelly V M 2020 Glow discharge-optical emission spectroscopy for *in situ* analysis of surfaces in plasmas *J. Vac. Sci. Technol.* A **38** 063004

[20] Onishi H, Yamazaki F, Hakozaki Y, Takemura M, Nezu A and Akatsuka H 2021 Measurement of electron temperature and density of atmospheric-pressure non-equilibrium argon plasma examined with optical emission spectroscopy *Jpn. J. Appl. Phys.* **60** 026002

[21] Bibinov N, Halfmann H, Awakowicz P and Wiesemann K 2007 Relative and absolute intensity calibrations of a modern broadband echelle spectrometer *Meas. Sci. Technol.* **18** 1327–37

[22] d'Agostino R, Cramarossa F, De Benedictis S and Ferraro G 1981 Spectroscopic diagnostics of CF_4-O_2 plasmas during Si and SiO_2 etching processes *J. Appl. Phys.* **52** 1259–65

[23] Fuller N C M, Herman I P and Donnelly V M 2001 Optical actinometry of Cl_2, Cl, Cl^+, and Ar^+ densities in inductively coupled Cl_2–Ar plasmas *J. Appl. Phys.* **90** 3182–91

[24] Kajita S, Asaoka K, Tanaka H, Nishio R, Tsutsumi T, Hori M and Ohno N 2020 Atomic nitrogen density measurements by actinometry method in the toroidal device NAGDIS-T *Jpn. J. Appl. Phys.* **59** 086002

[25] Greb A, Niemi K, O'Connell D and Gans T 2014 Energy resolved actinometry for simultaneous measurement of atomic oxygen densities and local mean electron energies in radio-frequency driven plasmas *Appl. Phys. Lett.* **105** 234105

[26] Kechkar S, Babu S K, Swift P, Gaman C, Daniels S and Turner M 2014 Investigation of absolute atomic fluorine density in a capacitively coupled SF_6/O_2/Ar and SF_6/Ar discharge *Plasma Sources Sci. Technol.* **23** 065029

[27] Booth J P and Sadeghi N 1991 Oxygen and fluorine atom kinetics in electron cyclotron resonance plasmas by time-resolved actinometry *J. Appl. Phys.* **70** 611–20

[28] Walkup R E, Saenger K L and Selwyn G S 1986 Studies of atomic oxygen in O_2+CF_4 rf discharges by two-photon laser-induced fluorescence and optical emission spectroscopy *J. Chem. Phys.* **84** 2668–74

[29] Lopaev D V, Volynets A V, Zyryanov S M, Zotovich A I and Rakhimov A T 2017 Actinometry of O, N and F atoms *J. Phys. Appl. Phys.* **50** 075202

[30] Caplinger J E, Perram G P and Adams S F 2021 A combined actinometry approach for medium pressure N_2—O_2 plasmas *Plasma Sources Sci. Technol.* **30** 015008

[31] Zhu Y, Lepikhin N D, Orel I S, Salmon A, Klochko A V and Starikovskaia S M 2018 Optical actinometry of O-atoms in pulsed nanosecond capillary discharge: peculiarities of kinetics at high specific deposited energy *Plasma Sources Sci. Technol.* **27** 075020

[32] Conway J, Kechkar S, O' Connor N, Gaman C, Turner M M and Daniels S 2013 Use of particle-in-cell simulations to improve the actinometry technique for determination of absolute atomic oxygen density *Plasma Sources Sci. Technol.* **22** 045004

[33] Karakas E, Donnelly V M and Economou D J 2013 Abrupt transitions in species number densities and plasma parameters in a CH_3F/O_2 inductively coupled plasma *Appl. Phys. Lett.* **102** 034107

[34] LXCat CDAP database 2024 (available at: www.lxcat.net/CDAP)

[35] Wang Y-F and Zhu X-M 2023 An optical emission spectroscopy method for determining the electron temperature and density in low-temperature xenon plasma by using a collisional-radiative model considering the hyperfine structure of emission line into metastable state *Spectrochim. Acta* B **208** 106777

[36] Zhu X-M, Cheng Z-W, Pu Y-K and Czarnetzki U 2016 Escape factors for Paschen 2p–1s emission lines in low-temperature Ar, Kr, and Xe plasmas *J. Phys. D: Appl. Phys.* **49** 225204

[37] Cosby P C 1993 Electron-impact dissociation of oxygen *J. Chem. Phys.* **98** 9560

[38] Zipf E C and Melaughlin R W 1978 On the dissociation of nitrogen by electron impact and by E.U.V. photo-absorption *Planet Space Sci.* **26** 449

[39] Filippelli A R, Sharpton F A, Lin C C and Murphy R E 1982 Production of atomic nitrogen emission by electron-impact dissociative excitation of nitrogen molecules *J. Chem. Phys.* **76** 3597–606

[40] Wang Y, Zatsarinny O and Bartschat K 2014 B-spline R-matrix-with-pseudostates calculations for electron-impact excitation and ionization of nitrogen *Phys. Rev.* A **89** 062714

[41] NIST Atomic Spectra Database 2023 (available at: http://nist.gov/pml/atomic-spectra-database)

[42] Guerra V, Sá P A and Loureiro J 2004 Kinetic modeling of low-pressure nitrogen discharges and post-discharges *Eur. Phys. J. Appl. Phys.* **28** 125–52

[43] Guerra V, Tatarova E and Ferreira C M 2002 Kinetics of metastable atoms and molecules in N_2 microwave discharges *Vacuum* **69** 171–6
[44] Zhu X-M, Pu Y-D, Guo Z-G and Pu Y-K 2006 A novel method to determine electron density by optical emission spectroscopy in low-pressure nitrogen plasmas *Phys. Plasmas* **13** 123501
[45] Gordiets F, Ferreira C M, Guerra V L, Loureiro J, Nahorny J, Pagnon D, Touzeau M and Vialle M 1995 Kinetic model of a low-pressure N_2-O_2 flowing glow discharge *IEEE Trans. Plasma Sci.* **23** 750–68
[46] Chilton J E, Stewart M D and Lin C C 2000 Cross sections for electron-impact excitation of krypton *Phys. Rev.* A **62** 032714
[47] Allan M, Zatsarinny O and Bartschat K 2011 Electron impact excitation of the ($4p^5 5s$) states in krypton: high-resolution electron scattering experiments and *B*-spline *R*-matrix calculations *J. Phys. B: At. Mol. Opt. Phys.* **44** 065201
[48] Kolts J H and Setser D W 1978 Decay rates of Ar($4s$, $^3P_2$), Ar($4s'$, ^3P), Kr(5s, $^3P_2$), and Xe(6s, $^3P_2$) atoms in argon *J. Chem. Phys.* **68** 4848
[49] Meng S, Zhu X, Kang Y, Wang Y, Ning Z and Yu D 2022 Investigation on the radial distribution of electron density in a miniaturized ECR ion thruster of wide-range operations *Vacuum* **202** 111138
[50] Itikawa Y 2006 Cross sections for electron collisions with nitrogen molecules *J. Phys. Chem. Ref. Data* **35** 31–53
[51] Straub H C, Renault P, Lindsay B G, Smith K A and Stebbings R F 1996 Absolute partial cross sections for electron-impact ionization of H_2, N_2, and O_2 from threshold to 1000 eV *Phys. Rev.* A **54** 2146–53
[52] Kleine C, Winghart M-O, Zhang Z-Y, Richter M, Ekimova M, Eckert S, Vrakking M J J, Nibbering E T J, Rouzée A and Grant E R 2022 Electronic state population dynamics upon ultrafast strong field ionization and fragmentation of molecular nitrogen *Phys. Rev. Lett.* **129** 123002
[53] Fierro A, Moore C, Yee B and Hopkins M 2018 Three-dimensional kinetic modeling of streamer propagation in a nitrogen/helium gas mixture *Plasma Sources Sci. Technol.* **27** 105008
[54] Bílek P, Kuthanová L, Hoder T and Šimek M 2022 Atmospheric pressure Townsend discharge in pure nitrogen—a test case for $N_2(A^3\Sigma+$ u, v) kinetics under low E/N conditions *Plasma Sources Sci. Technol.* **31** 084004
[55] Peters C J, Shneider M N and Miles R B 2019 Kinetics model of femtosecond laser ionization in nitrogen and comparison to experiment *J. Appl. Phys.* **125** 243301
[56] Li Q, Zhu W-C, Zhu X-M and Pu Y-K 2010 Effects of Penning ionization on the discharge patterns of atmospheric pressure plasma jets *J. Phys. D: Appl. Phys.* **43** 382001
[57] Koizumi H and Kuninaka H 2010 Miniature microwave discharge ion thruster driven by 1-watt microwave power *J. Propul. Power* **26** 601–4
[58] Xia X, Yang J, Jin Y, Hang G, Fu Y and Hu Z 2020 The influence of magnetic circuit and operating parameters on the plasma property of 2 cm ECRIT ion source *Vacuum* **179** 109517
[59] Zhu X-M, Wang Y-F, Meng S-F, Wang Y, Ning Z-X, Yu D-R and Bartschat K 2023 A xenon collisional-radiative model applicable to electric propulsion devices: III. Determination of the ionization fraction in low-temperature xenon plasma by using ionic and atomic 6p lines *Plasma Sources Sci. Technol.* **32** 095019
[60] Takao Y, Koizumi H, Komurasaki K, Eriguchi K and Ono K 2014 Three-dimensional particle-in-cell simulation of a miniature plasma source for a microwave discharge ion thruster *Plasma Sources Sci. Technol.* **23** 064004
[61] Kwon D-C, Yu D-H, Kwon H, Im Y H and Lee H-C 2020 Global model for pulsed inductively coupled plasma sources: effect of edge-to-center density ratio and electron heating *Phys. Plasmas* **27** 073507
[62] Coche P, Guerra V and Alves L L 2016 Microwave air plasmas in capillaries at low pressure I. Self-consistent modeling *J. Phys. D: Appl. Phys.* **49** 235207
[63] Stancu G D, Leroy O, Coche P, Gadonna K, Guerra V, Minea T and Alves L L 2016 Microwave air plasmas in capillaries at low pressure II. Experimental investigation *J. Phys. D: Appl. Phys.* **49** 435202
[64] Hu C, He L, Chen Y, Zhao B, Jun D and Qu M J 2021 Electrical and optical characterizations of a rotating gliding arc plasma-enhanced combustion dome in an aero-engine combustor *J. Phys. D: Appl. Phys.* **54** 205202
[65] Mumma M J and Zipf E C 1971 Dissociative excitation of vacuum-ultraviolet emission features by electron impact on molecular gases. II. N_2 *J. Chem. Phys.* **55** 5582–8
[66] LXCat Biagi database 2023 (available at: www.lxcat.net/Biagi) (Accessed 19 December 2023)